

國立交通大學

電子工程學系電子研究所

博士論文

光子晶體波導內的慢光現象及
整合型光子晶體面射型雷射之研究

Study on Slow Light in Photonic Crystal Waveguides
and Integrated Photonic Crystal Nanocavity Coupled
Surface Emitting Lasers

研究生：黃世傑

指導教授：李建平博士

中華民國九十六年六月

光子晶體波導內的慢光現象及
整合型光子晶體面射型雷射之研究

Study on Slow Light in Photonic Crystal Waveguides
and Integrated Photonic Crystal Nanocavity Coupled
Surface Emitting Lasers

研究生：黃世傑
指導教授：李建平 博士

Student : Shih-Chieh Huang
Advisor: Dr. Chien-Ping Lee

國立交通大學

電子工程學系電子研究所

博士論文

A Dissertation
Submitted to Institute of electronics
College of Electrical and Computer Engineering
National Chiao Tung University
in partial Fulfillment of the Requirements
for the Degree of
Doctor of Philosophy
in
Electronics Engineering
June 2007
Hsinchu, Taiwan, Republic of China

中華民國九十六年六月

光子晶體波導內的慢光現象及 整合型光子晶體面射型雷射 之研究

研究生:黃世傑

指導教授:李建平 博士

國立交通大學

電子工程學系暨電子研究所



在本論文中，我們報告兩種利用光子晶體所製造的光電元件。由於光子晶體本身的特殊能帶結構，使得這兩種光電元件具有特殊的性能，被認為會對未來多功能的光積體電路發展有所幫助。

首先，第一種元件是一種能讓光的傳輸速度減慢的光波導元件。我們設計了特殊的光子晶體波導，使得在波導內的傳輸光其群速度能大幅度的被減慢，這種現象稱為慢光。第二種元件是一種整合式的面射型雷射。我們將光子晶體共振腔整合在傳統的邊射型半導體雷射，使產生的雷射光耦合到光子晶體共振腔，並由其表面射出單一模態的雷射光。上述的這兩種光電元件，將會是未來發展多功能光積體電路中的重要關鍵元件。

在慢光的研究部分，我們首先設計了單一線缺陷的光子晶體波導（亦稱為W1型）來瞭解光波在其內部傳輸的行為模式。我們所製作的W1型光子晶體波導具有非常低的傳輸損失率(2dB/mm)。我們在其所量測到的頻譜圖上，觀察到在頻譜截斷區域的Fabry-Perot振盪週期迅速變小。將此異常週期代入Fabry-Perot

公式，可得到異常大的群折射率(200~300)。同時我們也利用時間領域的方法將 3GHz 的調變訊號導入 W1 型波導中，並量測其相位變化，間接推得光訊號再頻譜截斷區域有非常長的傳輸延遲時間。我們並將此測到的實驗數據與從能帶圖上計算得到的群速度理論值作了比較，發現這種的慢光現象是由於 W1 型光子晶體波導在 1st Brillouin zone 中，能帶邊緣的缺陷模態所造成。

根據上述由 W1 型光子晶體波導所得到的結果，我們更進一步研究一種具有特殊能帶結構的光子晶體耦合型波導。自此類型波導元件中，其光子能帶係內存在著一種 S 型的耦合缺陷能帶，此能帶有利於慢光現象的觀察。我們利用了 Mach-Zehnder 干涉方法所得到的光波群速度對頻率響應圖，證明了在那特殊 S 型耦合能帶上，的確存在一種異於能帶邊緣的慢光模態，我們稱之為轉折點型慢光模態。同時，我們也利用高速示波器來紀錄光波在此耦合型波導傳輸中，波形隨著時間變化的情形。藉由調整入射光的頻率，使其慢慢趨近耦合缺陷模態的頻率，我們觀察到逐漸增加的傳輸延遲時間，經由換算，我們得到了一個極小光波群速度，只有 $0.017c$ 。從能帶圖上所推得的群速度理論值也符合了我們所量測的結果。

在光子晶體共振腔部份，我們展示了一種整合型的奈米共振腔-雷射結構。在這結構中，由注入電流產生的雷射光會直接耦合到光子晶體共振腔，並從共振腔表面射出單一模態雷射光。同時藉由頻譜圖的分析，我們可到此光子晶體共振腔具有高品質因子(Q-factor)。另外，我們也觀察到從此共振腔射出的雷射光對溫度具有高性能的穩定性，此特徵值是一般量子井半導體雷射的 5 倍。最後，我們設計了兩個並肩型的光子晶體共振腔雷射，展示多重波長同時射出可能性。

Study on Slow Light in Photonic Crystal Waveguides and Integrated Photonic Crystal Nanocavity Coupled Surface Emitting Lasers

Student: Shih-Chieh Huang

Advisor: Dr. Chien-Ping Lee

Department of Electronics Engineering & Institute of Electronics Engineering

National Chiao Tung University



In this dissertation, two optoelectronic devices based on photonic crystals are presented. These two devices with their unique properties derived from the special band structure of the photonic crystals will be useful for future photonic integrated circuits with multiple functions.

The first device is an optical delay line that slows down the speed of the propagation light. A special waveguide based on line-defects in photonic crystal was designed to support waveguide mode with a significantly reduced group velocity. The second device is an integrated surface emitting laser. A regular in-plane laser was integrated with an photonic crystal nanocavity to couple the laser emission into a single mode surface emitting light. Both devices will be the key components for multi-function photonic integrated circuits.

In the part of slow light, single line defect (W1 type) photonic crystal

waveguides are first studied in order to understand the behaviors of propagation light over them. Very low propagation loss ($\sim 2\text{dB/mm}$) of the fabricated waveguides is obtained. The rapidly diminishing Fabry–Perot oscillation periods at the cutoff region of the measured transmission spectrum determine extremely large group indices of 200~300. The group delay time measurements by detecting phase shift of 3G Hz modulated signals through the waveguides also show a very large time-delay ($>200\text{psec}$) near the cutoff. In comparison with theoretical group velocities derived from the band structure, these experimental results are ascribed to the effect of the defect modes at the band edge of the first Brillouin zone.

Based on successful results of single line defect waveguides, we further investigate a photonic crystal coupled waveguide, where the unique guided mode band structure has a flat band region within the photonic band gap allowing for slow light observation. The spectral dependence of group velocity, which is measured by Mach-Zehnder interference method, indicates the existence of slow light modes around the inflection point of the unique flat band, rather than at the band edge. Time-domain observation of optical pulses propagating along two-dimension slab photonic crystal coupled waveguides is also demonstrated by using a high speed oscilloscope. By adjusting the wavelength of the input pulses toward the flat band of the coupled defect modes, an increasing duration time between reference and output pulses are clearly observed. An extremely small group velocity of $0.017c$ is thus obtained. Calculated group velocities show good agreement with our measured results.

In the part of photonic crystal nanocavity lasers, we demonstrate an integrated nanocavity laser structure, where the laser light is directly coupled to photonic crystal nanocavities (H1 and H2) and emits out from the surface with selected wavelengths of the resonant modes of the nanocavities. Single mode emission with high Q factors

[Q(H1)=1890 and Q(H2)=3800] is obtained with electrical pumping. Excellent temperature stability ($0.097\text{nm}/^{\circ}\text{C}$) of laser emission from the nanocavity is observed as well. The wavelength shift versus temperature is about five times better than that of regular quantum well lasers. Dual wavelength emission from two side-by-side photonic crystal nanocavities is also demonstrated.



Acknowledgements

I wish to express immense gratitude to my advisor, Prof. Chien-Ping Lee, for his enlightening teaching on quantum physics and optical devices during my graduate year at National Chiao Tung University, and for his guidance and encouragement over the frustrations I had suffered from my research process. I would love to give great thanks to my department, Department of Electronic Engineering, and my university, National Chiao Tung University, together with all the staff I had been in touch with, not only for the essential grants which made this doctoral degree possible, but also for their resourceful assistance.

As part of this research was conducted in NTT (Nippon Telegraph and Telephone Corporation) of Japan, I should first thank NSC (National Science Council) of Taiwan and NTT Basic Research Laboratories of Japan for their financial support during this period, with the former sponsoring the first year and the latter the following half year. I am grateful that Dr. Masaya Notomi offered such opportunity of internship and there led me to explore all the possible exciting aspects of photonic crystals. I appreciate Dr. Shinya, Dr. Taniyama, Dr. Tanabe, Dr. Kuramochi, Dr. Tawara, and Dr. Kato for their helpful suggestions. I am thankful to Prof. Yong-Hang Zhang from Arizona State University for giving advices on measurement systems during his visit to NTT. I especially thank Mr. Kondo, Mr. Morita, Mr. Sasaki, Mr. Tanaka, Mr. Chikamori, and all the friends there for introducing Japanese culture and teaching me Japanese. I am indebted to Prof. Chin-Fa Yeh, Director of Science and Technology Division of Taipei Economic and Cultural Representative Office in Japan, for his warm care at that time.

I owe great deal to Prof. Jong-Ching Wu at National Changhua University of

Education, who patiently taught me advanced nanotechnology. I acknowledge Dr. Sheng-Di Lin, Dr. Gray Lin, Dr. Su-Wei Chiou, Dr. Chien-Chi Lee, Dr. Bin-Chi Lee, and Dr. Po-Tsung Lee at National Chiao Tung University for their valuable discussions. I also deeply thank my research group members at National Chiao Tung University, including the graduated and present, for their hearty companionship throughout these years. Finally, to my family and friends, my gratitude is beyond words.



CONTENTS

ABSTRACT (Chinese)	i
ABSTRACT (English)	iii
ACKNOWLEDGMENTS	vi
CONTENTS	viii
TABLE CAPTIONS	xi
FIGURE CAPTIONS	xii

CHAPTER 1 INTRODUCTION

1.1 History of Photonic Crystals.....	1
1.2 Background and Motivation	4
1.3 Organization of Dissertation.....	6



CHAPTER 2 COMPUTATIONAL METHOD

2.1 Full Maxwell's Equations	8
2.2 Plane Wave Expansion Method.....	11
2.3 Photonic Band Structure	14
2.4 Supercell Techniques	17
2.5 Finite-Difference Time-Domain Method.....	19

CHAPTER 3 BAND-EDGE SLOW LIGHT MODES IN

TWO-DIMENSIONAL SLAB PHOTONIC CRYSTAL

WAVEGUIDES

3.1 Introduction.....	22
-----------------------	----

3.2 Band Diagram	25
3.3 Device Fabrication and Characterization.....	27
3.4 Group Velocity Measurement.....	32
3.4.1 Frequency-Domain Method.....	32
3.4.2 Time-Domain Method	35
3.5 Discussion.....	37
3.4 Summary.....	38

**CHAPTER 4 INFLECTION-POINT SLOW LIGHT MODES IN PHOTONIC
CRYSTAL COUPLED WAVEGUIDES**

4.1 Introduction.....	40
4.2 Band Structures of Photonic Crystal Coupled Waveguides	41
4.3 Fabrication of Photonic Crystal Coupled Waveguides.....	43
4.4 Spectral-Domain Measurement	45
4.5 Time-Domain Measurement.....	49
4.6 Summary.....	56

**CHAPTER 5 ELECTRICALLY-DRIVEN INTEGRATED PHOTONIC
CRYSTAL NANOCAVITY COUPLED SURFACE EMITTING
LASERS**

5.1 Introduction.....	57
5.2 Fabrication of Photonic Crystal Nanocavity Lasers	59
5.3 Nanocavity Design.....	63
5.4 Characterisitcs of Nanocavity Lasers.....	66
5.5 Summary.....	73

CHAPTER 6 CONCLUSION AND SUGGESTION

6.1 Conclusion74
6.2 Suggestion for Future Work.....75

REFERENCE.....78

VITA.....84

PUBLICATION LIST85



TABLE CAPTIONS

CHAPTER 4

Table 4.1 Structural parameters of photonic crystal coupled waveguides.



FIGURE CAPTIONS

CHAPTER 2

- Fig. 2.1 Schematic of a 2D photonic crystal structure with triangular lattices.
Fig. 2.2 Band diagram for the TE-like modes of a 2D triangular lattice structure.
Fig. 2.3 Concept of the supercell technique.
Fig. 2.4 Illustration of the Yee's cell used for FDTD method.

CHAPTER 3

- Fig. 3.1 Schematic of a W1 type photonic crystal waveguide, band structure and magnetic fields of defect waveguide modes.
Fig. 3.2 SEM micrographs of the fabricated W1 type photonic crystal waveguides.
Fig. 3.3 Schematic of the measurement system.
Fig. 3.4 Transmission spectrum of a W1 type photonic crystal waveguide with 54 μ m length.
Fig. 3.5 Measured spectra of the samples with different waveguide lengths.
Fig. 3.6 Transmittance against photonic crystal waveguide lengths at different launched wavelengths.
Fig. 3.7 Propagation loss spectrum for the fabricated W1 type photonic crystal waveguides.
Fig. 3.8 Group index dispersion curve.
Fig. 3.9 Magnified dispersion curve for the guided modes around the band-edge region and illustration of the Fabry-Perot resonant modes.
Fig. 3.10 Illustration of the phase-delay measurement setup.
Fig. 3.11 Measured group delay time curves.

CHAPTER 4

- Fig. 4.1 Band structure of photonic crystal coupled waveguides.
Fig. 4.2 SEM image of photonic crystal coupled waveguides.
Fig. 4.3 Simulated and fabricated MMI devices.
Fig. 4.4 Two kinds of interfaces: Type I and Type II.

- Fig. 4.5 Measured transmission spectrum of a photonic crystal coupled waveguide with length $L=200\mu\text{m}$.
- Fig. 4.6 Measured spectra for Type I and Type II.
- Fig. 4.7 Schematic of an integrated MZI structure and measured spectrum.
- Fig. 4.8 Schematic diagram of the experimental setup.
- Fig. 4.9 Time-resolved measurements obtained by recording output pulses on the oscilloscope.
- Fig. 4.10 Transmission spectra of input pulse and measured output signals.
- Fig. 4.11 Measured group velocities and group velocity dispersion in comparison with theoretical ones.

CHAPTER 5

- Fig. 5.1 Strained InGaAs/GaAs single quantum well laser structures.
- Fig. 5.2 Process flow of integrated photonic crystal nanocavity lasers.
- Fig. 5.3 Schematic of an integrated nanocavity coupled emitting laser.
- Fig. 5.4 SEM micrographs of completed photonic crystal patterns.
- Fig. 5.5 Calculated position dependence of coupled output light intensity from H1 nanocavity.
- Fig. 5.6 Resonant cavity modes calculated by 2D FDTD method.
- Fig. 5.7 Coupled cavity modes simulated by 2D PWE and FDTD methods.
- Fig. 5.8 (a) SEM picture of the fabricated sample with an integrated H1 cavity. (b) Infrared image taken from the H1 cavity. (c) Emission spectrum from the H1 cavity.
- Fig. 5.9 Emission spectra measured from the cleaved facet of the laser with the integrated H1 cavity at different bias condition.
- Fig. 5.10 For comparison, emission spectra from the H1 cavity and cleaved facet are put together.
- Fig. 5.11 L-I curves of laser emission from the H1 and H2 cavities.
- Fig. 5.12 Measured spectra of the H1 and H2 nanocavities
- Fig. 5.13 Emission spectra measured from the regular QW laser at different operation temperature.
- Fig. 5.14 Temperature dependence of the peak wavelength of the laser light measured from an H1 nanocavity and that of the regular laser light measured from the cleaved facet.
- Fig. 5.15 Resonant wavelength as a function of holes radius in modified H2 cavities and measured spectrum of the laser light from the two nanocavities.

Chapter 1

Introduction

1.1 History of Photonic Crystals

Photonic crystals are a new type of optical material having periodic variations of dielectric constants on the order of an optical wavelength. They are considered as an essential element for the development of all-photonics integrated circuits because of their excellent ability to manipulate and tailor the light. The concept of photonic crystal was first presented on *Physical Review Letters* in 1987 [1-2]. At that time, E. Yablonovitch proposed an idea of photonic band gap, analogous to the electron band gap, where no photon density exists so that the spontaneous emission corresponding to the gap energy is rigorously forbidden in all directions [1]. S. John, nearly at the same time, also found that the phenomena of strong localization of photons, similar to Anderson localization in electronic systems, could be observed in certain disordered superlattice microstructures with sufficiently high dielectric contrast [2], which are namely photonic crystal defect structures today.

Following these papers, many theoretical researchers started to work on the calculation of photonic crystal structures to figure out what kinds of patterns are applicable and how large the refractive index contrast is needed for constructing a complete photonic band gap. Most of them made use of the ideas from solid-state physics to simulate light behaviors in the periodically-arranged dielectric medium. By applying periodic boundary conditions to the four well-known Maxwell equations, the researchers obtained the eigenvalue equations, which bear resemblance to the

Schrödinger wave equations for electrons, and then proceeded to calculate band diagrams. This approach, called *plane wave expansion* method [3], became widely used by today's researchers. Their results, for the first time, showed the existence of a widely complete band gap in a diamond structure.

Apart from theories, the early experiments on the photonic band structures were confined only to the samples with millimeter-order periodicity because of limited fabrication support. E. Yablonovitch and his coworkers introduced a fully three-dimensionally (3D) periodic face-center-cubic structure, named as *Yablonovite*, and carried it out in the microwave region by directly drilling into a commercial and low loss dielectric material [4]. Their measured transmission data fit well with the theoretical band diagrams. This was the first verified experiment on a complete photonic band gap. According to the scaling properties of the Maxwell equations, the work also indicated that the fabrication of 3D photonic crystals with submicron periodicity in the visible or near-infrared region is possible. Therefore, in the later half of the 1990s, with the help of gradually maturing nanotechnology, various 3D crystal structures with a complete band gap, such as woodpile or stacked strip structure, were sequentially demonstrated in the optical communication wavelength range [5, 6].

Meanwhile, two-dimensional (2D) photonic crystals were also continued to be developed. They are thought of having advantages of easy fabrication and flexible integration over 3D crystal structures. But, the finite thickness in one dimension makes propagation light decoupled into two separate polarizations, TM and TE modes. Here TM is the magnetic field lying in the 2D crystal plane and TE is the magnetic field emitting out of the plane. So, two different kinds of band diagrams need to be concerned. MIT group theoretically pointed out the existence of 2D photonic band gap, where TE and TM mode gaps overlapped each other, by optimizing air hole radius of triangular lattice in a dielectric substrate ($\epsilon=13$) [7]. Then, T. F. Krauss et al.

demonstrated a high-aspect-ratio 2D crystal structure by etching holes into GaAs based substrate [8], and subsequently proved the polarization-dependent photonic band gaps in near-infrared range by utilizing a waveguide configuration [9]. Till the end of the 1990s, the studies of 2D photonic crystals mostly concentrated on the achievement of sufficient depth of etching holes on semiconductor materials so as to observe photonic band gap effect.

In 1999, Caltech research team used a 2D slab structure to successfully demonstrate laser emission from photonic crystal nanocavity [10]. The slab structure was designed to have a thin thickness of $\lambda/2n$, where λ is the wavelength of light in vacuum and n is the refractive index of dielectric materials, to meet the fundamental mode of standing waves, and was sandwiched by air at the upper and bottom sides to make index contrast large so that strong optical confinement in the direction perpendicular to the 2D crystal plane could be achieved. This report greatly attracted scientists' and engineers' attention because of its potential in realization of planar monolithic optical integrated circuits. In 2000, Noda et al. carried out a preliminary photonic crystal circuit, where a point defect cavity is incorporated with a line defect waveguide, in Si-based photonic crystal slab structure [11]. They found that propagation light through the photonic crystal waveguide can be trapped by the nearby cavity and then emitted to the outside world. This discovery opened up a new way for design of all-optical functional devices, such as channel add/drop filters, optical switches and so on. Since then, scientists and engineers gradually shifted their research directions from the early investigation of 3D full band gaps to the development of multi-functional 2D slab structures.

Accompanying these are many interesting physical phenomena, which are either anticipated or observed in a variety of novel experiments and in the numerical simulations related to the photonic band engineering. Russell's group demonstrated a

single mode photonic crystal fiber [12], where the fiber core is a large air hole and the clad is made of triangular array silica tubes. Such fiber has the advantage of suppression of nonlinear effect at high power. Notomi detailed light propagation characteristics in strongly modulated photonic crystal and found negative refractive index phenomenon from calculation results [13]. Yoshie et al. embedded quantum dots in photonic crystal slab nanocavities and observed vacuum-field Rabi splitting exceeding decoherence linewidths of both the nanocavity and the quantum [14]. Gersen et al. reported the real-space observation fast and slow pulses propagation in a photonic crystal waveguide by a time-resolved near-field scanning optical microscope [15]. Yanik and Fan proposed and analyzed a physical system, which is composed of square lattice photonic crystal cavities, for the purpose of stopping and storing light coherently [16].



1.2 Background and Motivation

Currently, the interest in photonic crystal waveguides and nanocavities is increasing and has two main developments: one is photonic crystal waveguides with broad transmission bandwidth, large propagation delay time, and small dispersion, the other is photonic crystal cavities with high Q factors and small volumes. The former has the property of slowing down the speed of light and the latter exhibits the potential for storing the optical signals. Both of them are considered the key components of optical buffer devices for the quantum information processing system.

Photonic crystal waveguides are created by removing one or several line defects from the otherwise lattices, thus forming the defect modes (or waveguide modes) within the photonic band gap. Since the group velocity of propagation waves in the

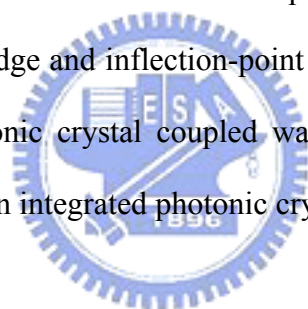
dielectric materials can be determined from the band structures by differentiating the corresponding dispersion curves (i.e. $V_g = d\omega/dk$), the guided modes in photonic crystal waveguides can propagate at extremely slow speed if their dispersion curves are properly designed. Such slow light guided modes in photonic crystal waveguides were first demonstrated by NTT research team in 2001 [17]. They observed the rapidly diminishing Fabry-Perot (FP) oscillation periods at the cutoff region of the measured transmission spectrum in W1 type photonic crystal waveguides (one row of line defect was removed). By applying FP formula, they obtained unusual large group index of $n_g \sim 100$. In other words, the speed of light is slowed down by about one hundred times than that in vacuum. Because these observed slow light guided modes exactly corresponded to the band-edge waveguide modes in the theoretical dispersion curves of the photonic crystal waveguides, they are named *band-edge slow light modes*.

In the following years, various experimental measurements on the band-edge slow light modes of W1 type photonic crystal waveguides were sequentially reported (see Section 4.1). Most of them used frequency-domain approaches to indirectly deduce group index. However, results from direct time-resolved measurements on the dynamical propagation waves are very limited because of large group-velocity-dispersion and narrow operation bandwidth for the band-edge slow light modes.

As for photonic crystal nanocavities with high Q factors and small volumes, a number of reports have shown that the ultra high Q nanocavities can be realized by a variety of delicate designs. Lee's group observed whispering gallery mode with Q value of 5,000 by optimizing the inner most holes of a point defect cavity [18]. Song et al. experimentally obtained extremely high Q factor of 600,000 using heterostructure nanocavity [19]. Later, Kuramochi and his coworkers demonstrated Q

value exceeding 800,000 by modulating the local width of a photonic crystal line defect waveguide [20]. However, these experiments are all carried out either by the use of optical pumping or by means of light coupling from a passive waveguide and an external light. Very little work has been done in the aspect of electrically pumping high-Q photonic crystal cavities because of difficulty in device fabrication.

The purpose of this dissertation is to investigate another type of slow light modes (named “inflection-point slow light modes”) with small group velocity and small group-velocity-dispersion in photonic crystal coupled waveguides by recording the dynamical propagation light waves on a high speed oscilloscope, and to fabricate the electrically-driven photonic crystal nanocavities by means of the integration with quantum well semiconductor laser diodes. Two topics are covered: (1) slow light phenomena, including band-edge and inflection-point slow light modes, in single line defect waveguides and photonic crystal coupled waveguides, and (2) single mode operation of electrically-driven integrated photonic crystal nanocavity coupled surface emitting lasers.



1.3 Organization of Dissertation

The dissertation is organized as follows.

Chapter 2 provides the theoretical fundamentals of photonic crystal structures. Propagation light wave within the periodic dielectric materials is discussed by the use of Maxwell equations. Plane wave expansion (PWE) method to solve the Maxwell equations is elucidated in the chapter. The concept of photonic band diagram and photonic band gap are then described with the help of eigenfunctions obtained from the method. The supercell technique employing on PWE method is introduced for the

analyses of photonic crystal defect structures. The widely-used finite difference time domain (FDTD) method to simulate dynamic field transition in photonic crystal is detailed as well.

In Chapter 3, we present the band-edge slow light modes in the single line defect photonic crystal waveguides. The propagation loss of the fabricated samples is evaluated by means of the cut-back method. The group index dispersion curve is obtained from the measured spectra by applying Fabry-Perot method. The increasing group delay time at the cutoff frequency is also observed in the phase-detection measurements and related with the band-edge defect modes of photonic crystal waveguides.

Following these results, 2D slab photonic crystal coupled waveguides with a unique flat band allowing inflection point slow light modes propagation are systematically studied in Chapter 4. The theoretical band structure is first designed to obtain S-shaped coupled band. Then, the existence of the coupled modes is examined by transmission spectra and Mach-Zehnder interference curves. Finally the time-resolved measurements on temporal optical pulses through the coupled waveguides are conducted.

In Chapter 5, we demonstrate an integrated photonic crystal nanocavity coupled laser structure. A practical fabrication process of photonic crystal nanocavity integrated with electrically driven quantum well laser diodes is successfully developed. Light emission from the nanocavity is observed and compared with that from the cleaved facet of the integrated laser diode. The temperature stability of the nanocavity modes and the capability of multiple wavelength emission from side by side slightly different nanocavities are also investigated, respectively.

The conclusion and suggestion for future work are found in Chapter 6.

Chapter 2

Computational Method

This chapter provides the theoretical fundamentals relevant to the study of photonic crystal structure. In the beginning, Maxwell equations will be introduced to discuss the propagation of light wave within a linear, isotropic, and homogeneous medium. Then, light behaviors in the periodic dielectric materials will be analyzed with the help of plane wave expansion (PWE) method. To determine field modes for a 2D photonic crystal, the photonic band diagram and the photonic band gap are elucidated. Besides, the supercell technique employing on the PWE method to solve defect crystal structures will also be described. Finally, the finite difference time domain (FDTD) method will be detailed to calculate the space and time changes in the electromagnetic fields of light.



2.1 Full Maxwell's Equations

According to the electromagnetic model, all the light waves are governed by four well-known **Maxwell equations** (SI units):

$$\nabla \cdot B = 0, \tag{2.1a}$$

$$\nabla \cdot D = \rho, \tag{2.1b}$$

$$\nabla \times E = -\frac{\partial B}{\partial t}, \tag{2.1c}$$

$$\nabla \times H = J + \frac{\partial D}{\partial t}. \tag{2.1d}$$

Here B , E , H , and D are the magnetic flux density, electric field, magnetic field and electrical displacement field, respectively. J is the free current density and ρ is the free

charges. These Maxwell's equations are generally applied to macroscopic averages of the fields, which vary wildly on a microscopic scale in the vicinity of individual atoms [21]. It is only in this averaged sense that one can handily treat light behaviors in various kinds of dielectric media. Detailed description of these equations from their microscopic correspondent can be found in [21-22].

Here let us consider a simple case of a uniform and transparent medium for propagation light. In this medium, no external light or current source is assumed. That is, J and ρ are all 0. We also restrict ourselves to the linear regime of the medium so that higher order terms of dielectric constant related to nonlinearity can be ignored here. To simplify the system, frequency dependence of dielectric constant is neglected. In addition, we treat this medium as a non-dispersive, isotropic, and lossless dielectric material. Therefore, D and B fields related to E and H can be given by

$$D(r) = \epsilon_0 \epsilon(r) E(r), \quad (2.2a)$$

$$B(r) = \mu_0 \mu(r) H(r). \quad (2.2b)$$

where $\epsilon(r)$ and $\mu(r)$ are the electrical permittivity (dielectric constant) and the magnetic permeability of the material, respectively. ϵ_0 and μ_0 denote the proportionality constants in vacuum and hold the relation of $\epsilon_0 \mu_0 = 1/c^2$, where c is the speed of light in vacuum. Since $\mu(r)$ is very close to unity for most dielectric materials of interest, we set $B(r) = \mu_0 H(r)$ in the following derivations.

With all of these assumptions done, the Maxwell's equations [(2.1a) ~ (2.1d)] are reduced to

$$\nabla \cdot H(r, t) = 0, \quad (2.3a)$$

$$\nabla \cdot \varepsilon(r)E(r, t) = 0, \quad (2.3b)$$

$$\nabla \times E(r, t) = -\mu_0 \frac{\partial H(r, t)}{\partial t}, \quad (2.3c)$$

$$\nabla \times H(r, t) = \varepsilon_0 \varepsilon(r) \frac{\partial E(r, t)}{\partial t}. \quad (2.3d)$$

Here $E(r, t)$ is the electric field and $H(r, t)$ is the magnetic flux density at the point r and time t . Since these equations are linear, we can separate out the time dependence by expanding the fields into a set of harmonic modes:

$$E(r, t) = E(r)e^{-i\omega t},$$

$$H(r, t) = H(r)e^{-i\omega t}.$$

Equation (2.3) then becomes

$$\nabla \cdot H(r) = 0, \quad (2.4a)$$

$$\nabla \cdot \varepsilon(r)E(r) = 0, \quad (2.4b)$$

$$\nabla \times E(r) = i\omega\mu_0 H(r), \quad (2.4c)$$

$$\nabla \times H(r) = -i\omega\varepsilon_0 \varepsilon(r)E(r). \quad (2.4d)$$

Now take a look at Eq. (2.4a) and (2.4b). They mean that the divergence of a magnetic field or electrical displacement field is always zero. If consider the propagation of a uniform plane wave along the arbitrary direction within the medium, we will find that a constant vector (amplitude) of the magnetic field (or electric field) is always transverse to the direction of propagation. Take a plane wave of a magnetic field $H(r) = H_0 e^{ik \cdot r}$ as an example [23]. Here H_0 is a constant vector, and k is a wavenumber vector and defined as $k = \mathbf{a}_x k_x + \mathbf{a}_y k_y + \mathbf{a}_z k_z = k \mathbf{a}_n$. r is a radius vector given by $r = \mathbf{a}_x x + \mathbf{a}_y y + \mathbf{a}_z z$. So, the plane wave $H(r)$ can be written compactly as $H(r) = H_0 e^{ik \cdot r} = H_0 e^{ik a_n r}$, where \mathbf{a}_n is a unit vector in the direction of propagation.

By replacing $H(r)$, the divergence equation of $\nabla \cdot H(r) = 0$ becomes

$$ik(H_0 \cdot a_n)e^{ika_n r} = 0$$

which requires $H_0 \cdot a_n = 0$. Similarly, we can also obtain the results of $E_0 \cdot a_n = 0$ by assuming a uniform plane wave of $E(r) = E_0 e^{ik \cdot r}$. Thus this proves that both E and H are transverse to the direction of propagation.

Based on reference [22], E and H are also shown perpendicular to each other in a homogenous, source-free, and lossless medium. Generally, we name such particular field configuration *transverse electromagnetic (TEM) wave*.

Next, we pay our attention to the last two curl equations, Eq. (2.4c) and (2.4d). These two equations can be combined together by taking the curl on both sides of the equations. Then the equations become entirely in $E(r)$ or $H(r)$:

$$\nabla \times \nabla \times E(r) = \left(\frac{\omega}{c}\right)^2 \varepsilon(r) E(r), \quad (2.5a)$$

or

$$\nabla \times \left[\frac{1}{\varepsilon(r)} \nabla \times H(r) \right] = \left(\frac{\omega}{c}\right)^2 H(r). \quad (2.5b)$$

using $\varepsilon_0 \mu_0 = 1/c^2$. It is now clear that the modes $E(r)$ or $H(r)$ for a specific frequency can be solved if a dielectric function $\varepsilon(r)$ is given.

2.2 Plane Wave Expansion Method

Since photonic crystal is a kind of periodically varied dielectric materials, its nature of highly symmetries in space, such as translational symmetry, rotational symmetry, mirror symmetry and so on [23-24], is helpful to shorten the calculation time as we determine field modes by Eq. (2.5a) or (2.5b). These special characteristics are very

similar to those of electron systems so that some of the theorems and terminologies of solid state physics can be inherited by photonic crystal in slightly modified forms. In the well-known Schrödinger equation for band calculations of electrons, for example, periodic Coulomb potential in crystals is expressed by Fourier expansion and an electron wave function is supposed in Bloch form [25-26]. When substituted into the Schrödinger equation, the allowed eigenstate of electron energy as a function of its kinetic momentum is thus solved. This approach is named *plane wave expansion (PWE)* method because an electron wave function expressed as a superposition of plane waves is used [3, 27-29].

The same derivation can be applied to the propagation of lightwaves in photonic crystals. The Coulomb potential of an electron is now replaced by the periodic dielectric constant $\varepsilon(r)$ and given by

$$\varepsilon(r) = \sum_G \varepsilon_G e^{iG \cdot r} \quad (2.6)$$

with $\varepsilon_G = \frac{1}{V_c} \int_{\text{unit cell}} \varepsilon(r) e^{-iG \cdot r} dV$,

where G is the reciprocal lattice vector to characterize the periodicity of photonic crystal and V_c is the volume of the unit cell. The wavefunction of an electric field $E(r)$ or magnetic field $H(r)$ can also be expressed in the form of the Bloch type, given by

$$E_k(r) = \sum_G \phi_k(G) e^{i(G+k) \cdot r}, \quad (2.7a)$$

$$H_k(r) = \sum_G h_k(G) e^{i(G+k) \cdot r}. \quad (2.7b)$$

Here $\phi_k(G)$ and $h_k(G)$ are unknown vector amplitudes of the plane wave $(k+G)$, which is to be determined so that $E_k(r)$ and $H_k(r)$ become solutions to Maxwell's equation [(2.5a) or (2.5b)], and their corresponding unit vectors are perpendicular to $(k+G)$ because of the transverse nature of H and D ($\nabla \cdot H(r) = 0 = \nabla \cdot D(r)$). k is an arbitrary wavevector within the first Brillouin zone (because any k located outside the

Brillouin zone can be replaced by $(k-G)$ without the results changed, as introduced in solid state physics [25-26]). Substituting Eq. (2.6) and (2.7) into Eq. (2.5), we obtain the following matrix [28-29]:

$$\begin{aligned}\nabla \times \nabla \times E(r) &= \left(\frac{\omega}{c}\right)^2 \varepsilon(r)E(r), \\ \Rightarrow (k+G) \cdot (k+G') \times \phi_k(G') &= \left(\frac{\omega}{c}\right)^2 \sum_{G'} \varepsilon_{G,G'} \phi_k(G').\end{aligned}\quad (2.8a)$$

$$\begin{aligned}\nabla \times \left[\frac{1}{\varepsilon(r)} \nabla \times H(r) \right] &= \left(\frac{\omega}{c}\right)^2 H(r), \\ \Rightarrow (k+G) \times \sum_{G'} \varepsilon_{G,G'}^{-1} (k+G') \times h_k(G') &= -\left(\frac{\omega}{c}\right)^2 h_k(G').\end{aligned}\quad (2.8b)$$

where $\varepsilon_{G,G'}$ and $\varepsilon_{G,G'}^{-1}$ are the Fourier coefficients of $\varepsilon(r)$ and $\varepsilon^{-1}(r)$ on the plane wave with wavevector $(G'-G)$. Both equations are the k -dependent linear matrixes and can be solved by using standard matrix-diagonalization method [29].

Futhermore, Eq. (2.8) indicates that the dielectric materials enter the calculation only through the position-dependent dielectric function $\varepsilon(r)$, which is evaluated on the fine grid in the real space of unit cell and Fourier transformed into the reciprocal space [3]. Therefore, any periodic arrangement of dielectric crystals with any shapes and filling ratios can be exactly treated in the calculation of field eigenmodes. This was first proposed by Ho et al. in 1990 and is noted for its efficiency and accuracy in calculation [3]. They used the calculated 750 plane waves for a 3D fcc dielectric structure and achieved eigenfrequency convergence within 1%. Today, of course, the improvement of the numerical approaches and the rapid development of computers have reduced a lot of time in calculating 3D crystal structures, which used to require thousands of plane waves for accuracy.

Although the PWE method has advantages of accuracy and efficiency, there are still two limitations. One is for *dispersive material* and the other is for *nonperiodic*

structure. The former contributes complex part to the dielectric function. This contradicts the assumption that the refractive index distribution must be identical at all frequencies of the modes being found. The alternative solution is to use FDTD method, which will be introduced in Section 2.5. The latter usually occurs when we treat defect structures but can be solved by employing *supercell technique*, which will be described in Section 2.4.

2.3 Photonic Band Structure

Since Eq. (2.8) is also a kind of Hermitian eigenvalue problems, all of the eigenvalues $(\omega/c)^2$ can be obtained for a given value of k [23, 29]. If we plot the eigen-frequency (ω) as functions of wavevectors (k) in the first Brillouin zone, the so-called photonic band structure would be obtained. Take a 2D photonic crystal structure as an example. Assume that the air crystal patterns are embedded in a dielectric background $\varepsilon(r)$ and arranged in hexagonal array. The radius of the crystal is r and the pitch (lattice constant) is a , as shown in Fig. 2.1(a). Because it is a two dimensional structure, there are only two primitive lattice vectors, \vec{a}_1 and \vec{a}_2 , in real space [26]. In this case, they are expressed by

$$\begin{aligned}\vec{a}_1 &= a\hat{x}, \\ \vec{a}_2 &= a\left(\frac{1}{2}\hat{x} + \frac{\sqrt{3}}{2}\hat{y}\right),\end{aligned}\tag{2.9}$$

which corresponds to the reciprocal lattice vectors

$$\begin{aligned}\vec{b}_1 &= \frac{2\pi}{a}\left(\hat{x} - \frac{1}{\sqrt{3}}\hat{y}\right), \\ \vec{b}_2 &= \frac{2\pi}{a}\frac{2}{\sqrt{3}}\hat{y},\end{aligned}\tag{2.10}$$

, as shown in Fig. 2.1(b). The relation between \vec{a}_1, \vec{a}_2 and \vec{b}_1, \vec{b}_2 is defined by $\vec{a}_i \cdot \vec{b}_j = 2\pi\delta_{ij}$, where i and j are integers. We then rewrite Eq. (2.6) and (2.7) as

$$\varepsilon_r(x, y) = \sum_m \sum_n \varepsilon_{m,n} e^{i\frac{2\pi m}{a}x} e^{i\frac{2\pi(2n-m)}{a\sqrt{3}}y}, \quad (2.11)$$

$$E_{x,y,z} = \sum_p \sum_q \phi_{p,q}^{E_{x,y,z}} e^{i\frac{2\pi p}{a}x} e^{i\frac{2\pi(2q-p)}{a\sqrt{3}}y} e^{i(k_x x + k_y y + k_z z)}, \quad (2.12)$$

by the use of Eq. (2.9) and (2.10) [29]. Here $m, n, p,$ and q are integers and $\varepsilon_{m,n}$ are Fourier coefficients and given by

$$\varepsilon_{m,n} = \frac{1}{V_{unit\ cell}} \iint \frac{1}{\varepsilon_r(x, y)} e^{-i\frac{2\pi m}{a}x} e^{-i\frac{2\pi(2n-m)}{\sqrt{3}a}y} dx dy. \quad (2.13)$$

$\phi_{p,q}^{E_{x,y,z}}$ represents Fourier coefficients of each electric field component and needs to be determined later.

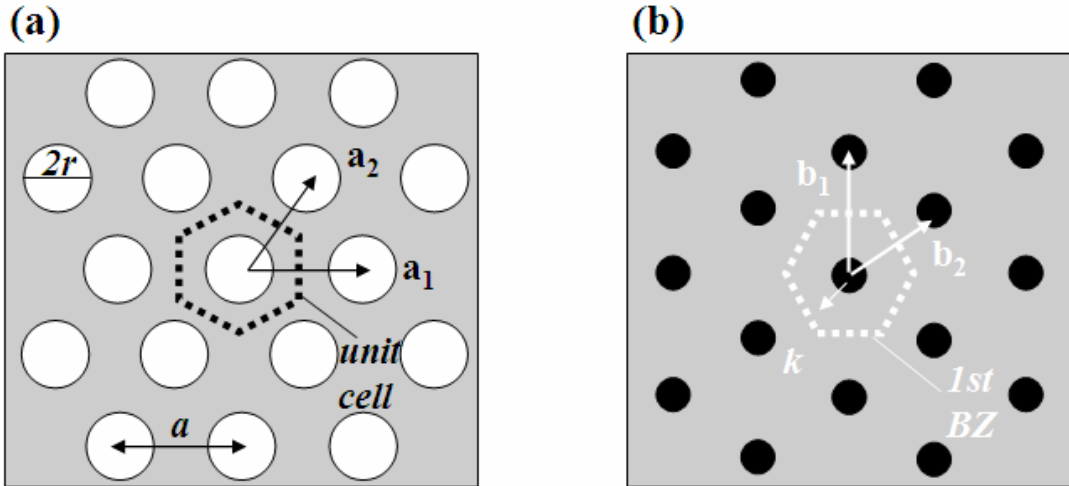


Fig. 2.1 Schematic of a 2D photonic crystal structure with triangular lattices. (a) Real lattice vectors, \vec{a}_1 and \vec{a}_2 , and a dielectric background $\varepsilon(r)$. (b) Reciprocal lattice vectors, \vec{b}_1 and \vec{b}_2 , and a wave vector \vec{k} .

Next, substituting Eq. (2.11) and (2.12) back into Eq. (2.5a) and performing a series of algebraic simplification, we can obtain a modified eigenvalue equation:

$$\sum_m \sum_n \varepsilon_{p-m, q-n} O \begin{bmatrix} \phi_{m,p}^{E_x} \\ \phi_{m,p}^{E_y} \\ \phi_{m,p}^{E_z} \end{bmatrix} = \frac{\omega^2}{c^2} \begin{bmatrix} \phi_{m,p}^{E_x} \\ \phi_{m,p}^{E_y} \\ \phi_{m,p}^{E_z} \end{bmatrix}, \quad (2.14)$$

where O is a matrix in which each entry is a function of wavevector k . (The step-by-step derivation of Eq. (2.14) can be found in [29].) Finally, the eigenfrequency ω as functions of k can be determined with the help of linear algebra and diagonalization.

Figure 2.2 shows the calculated dispersion curve ω - k (or named as photonic band diagram) of a 2D photonic crystal structure. In this case, the dielectric constant of air crystal and dielectric background are 1 and 13, respectively. The hole radius r is $0.33a$. Because the light wave now propagates in the xy plane, the filed modes are seperated into two distinct polarizations, TE-like (E in the xy plane) and TM-like (H in the xy plane) modes. Here, only TE-like modes are concerned.

From Fig. 2.2, we found a special mode gap in a certain frequency region. That is, the density of states, the number of possible modes per unit frequency, is zero within the region. So this gap is called the *photonic band gap*. All light emission and propagation are prohibited in it. Many applications of this property to nanocavity lasers and waveguides are rapidly developed. A good example will be detailed in Chapter 5. Also, Figure 2.2 reveals that the group velocity of light waves, defined by $d\omega/dk$, is zero at some symmetric points, like Γ and K . This is very interesting because as light speed is retarded, the photon-material interaction time will be extended; thus, the properties, such as optical gain and nonlinearity effect, would be enhanced. Such topic is categorized as slow light phenomenon and also the focus of this dissertation. More details can be seen in Chapter 3 and 4.

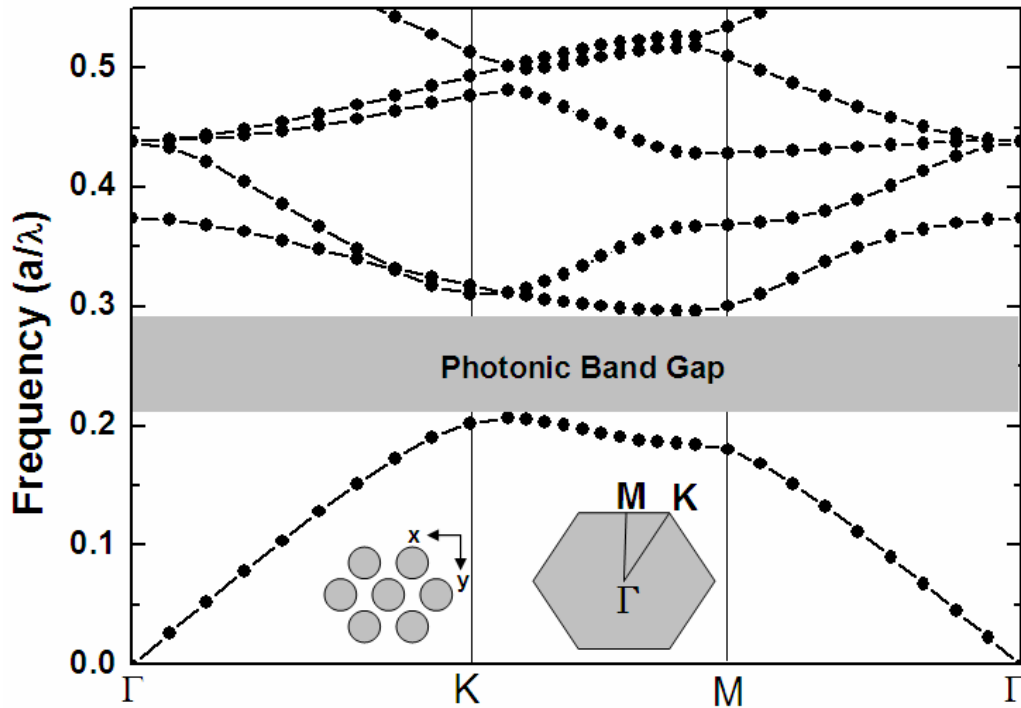
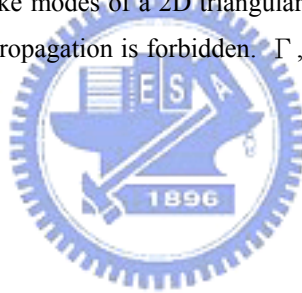


Fig. 2.2 Band diagram for the TE-like modes of a 2D triangular lattice structure. The gray area shows the photonic band gap where light propagation is forbidden. Γ , M, and K are symmetric points in the first Brillouin zone.



2.4 Supercell Techniques

Based on the PWE method (Eq. 2.8), infinite periodicity of dielectric materials in all directions is a requirement for band diagram and field mode calculation. However, if a defect is introduced into the otherwise periodic structures, the original periodicity of system would be altered and a defect mode would arise in the photonic band structure. To avoid this, the technique of “supercell” is often employed in PWE method. The approach is to replace the original unit cell of the structure by a complicated unit cell, where a defect is surrounded by a set of crystals. The new defined cell, called *supercell*, retains its periodicity in every direction so that PWE method can be applied to solve defect modes [28-29].

Figure 2.3 is an example of cavity defect modes calculated by a 5x5 supercell technique. The supercell size depends on design structures and user's demand, but it should be large enough to avoid interaction with adjacent supercell. Generally, the larger the supercell, the more accurate the defect states are and the longer the calculation time takes. In this case, only a single defect is concerned so that a small size of 5x5 supercell is used. If defect structures become complicated, such as several missing holes around crystals, larger cells are necessary for studying confined modes with higher accuracy. The same technique can be applied to photonic crystal slabs. These structures are periodic in two dimension (i.e. xy plane), but the dielectric function $\epsilon(r)$ in the third dimension (i.e. z direction) still varies because of the finite thickness of slab. If we are able to define an appropriate cell plane, the PWE method can be used.

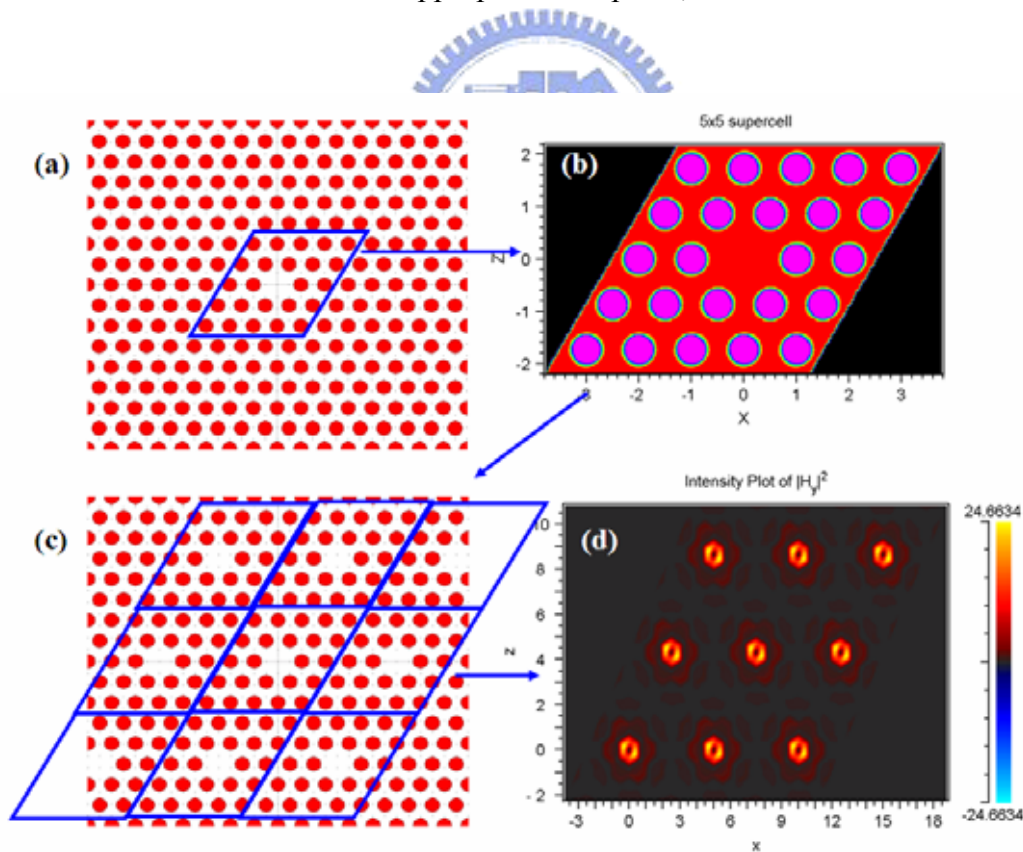


Fig. 2.3 Concept of the supercell technique. (a) A 2D photonic crystal defect structure. (b) A selected 5x5 supercell, including the defect. (c) Repeated supercell in all directions for the PWE method. (d) Calculated defect modes in each identical supercell. Clearly it is seen that no interaction occurs between two adjacent supercells.

2.5 Finite-Difference Time-Domain Method

Another widely used numerical technique for computing the propagation of light waves in the medium is the *finite-difference time-domain (FDTD)* method [30-32]. The FDTD method is a rigid solution to the Maxwell's equations. Different from the PWE method which merely provides stationary states (eigenmodes), the FDTD method can directly explore the dynamic motion of light waves. Besides, there is no theoretical restriction and approximations in the FDTD method. Any finite space including objects can be straightforward analyzed by the FDTD technique.

The main algorithm of FDTD method builds on solving two Maxwell's curl equations, as depicted in Eq. (2.3c) and (2.3d). If we rewrite the equations in Cartesian coordinates, we would obtain six scalar equations [33]:

$$\begin{aligned}
 \frac{\partial E_x}{\partial t} &= \frac{1}{\varepsilon} \left(\frac{\partial H_z}{\partial y} - \frac{\partial H_y}{\partial z} \right), & \frac{\partial H_x}{\partial t} &= -\frac{1}{\mu} \left(\frac{\partial E_z}{\partial y} - \frac{\partial E_y}{\partial z} \right), \\
 \frac{\partial E_y}{\partial t} &= \frac{1}{\varepsilon} \left(\frac{\partial H_x}{\partial z} - \frac{\partial H_z}{\partial x} \right), & \frac{\partial H_y}{\partial t} &= -\frac{1}{\mu} \left(\frac{\partial E_x}{\partial z} - \frac{\partial E_z}{\partial x} \right), \\
 \frac{\partial E_z}{\partial t} &= \frac{1}{\varepsilon} \left(\frac{\partial H_y}{\partial x} - \frac{\partial H_x}{\partial y} \right), & \frac{\partial H_z}{\partial t} &= -\frac{1}{\mu} \left(\frac{\partial E_y}{\partial x} - \frac{\partial E_x}{\partial y} \right).
 \end{aligned} \tag{2.15}$$

All of these equations indicate that any spatial variations of one field would cause the other field to change dynamically. In other words, the electric field and the magnetic field are interlaced in temporal and spacial domain. The FDTD techniques to solve the equations are based on Yee's approach published in 1966 [31]. Yee divided the analytical domain into small rectangular cells with edges $\Delta x = \Delta y = \Delta z$, and assumed that each E field vector component is located midway between a pair of H field vector components inside the cells (see Fig. 2.4), and vice versa. Then, he discreted the time step so that E and H field components can be computed at every short time interval Δt .

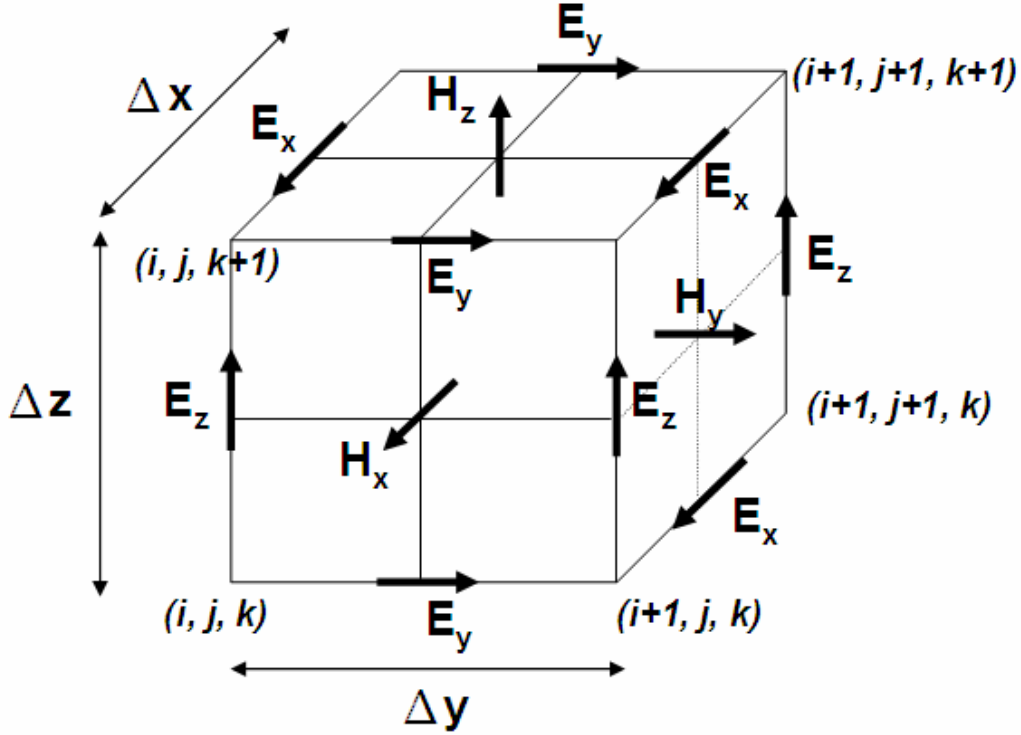


Fig. 2.4 Illustration of the Yee's cell used for FDTD method [31].

For example, the field components, E_z and H_z , in Eq. (2.15) at time $t = n\Delta t$ (n is an integer) can be solved by

$$E_{z(i,j,k)}^{n+1} = E_{z(i,j,k)}^n + \frac{\Delta t}{\epsilon\Delta x} (H_{y(i,j+1,k)}^{n+1/2} - H_{y(i,j,k)}^{n+1/2}) - \frac{\Delta t}{\epsilon\Delta y} (H_{x(i,j,k+1)}^{n+1/2} - H_{x(i,j,k)}^{n+1/2}),$$

$$H_{z(i,j,k)}^{n+1/2} = H_{z(i,j,k)}^{n-1/2} + \frac{\Delta t}{\mu\Delta y} (E_{x(i,j,k)}^n - E_{x(i,j,k-1)}^n) - \frac{\Delta t}{\mu\Delta x} (E_{y(i,j,k)}^n - E_{y(i,j-1,k)}^n),$$

if a cell, denoted by integers (i, j, k) , is given [33]. This scheme, now called Yee's cell or Yee's mesh, proves to be essential to many current FDTD softwares.

There is an important issue to be addressed while using FDTD method. It is *boundary condition*. In the real world, the space is continuous and infinite, but in the FDTD method, the computational domain is finite and limited by the computer memory. Therefore, as the light waves reach the boundary surface of the computational domain, reflection would occur and disturb the excited fields. To solve this problem, many simulations introduce an *absorbing boundary condition (ABC)*,

which eliminates any outward-going waves that impinge on the domain boundaries, into their models [33]. Among a number of available highly effective absorbing boundary conditions, *Mur's condition* and *Beregner's perfectly matched layer (PML)* condition are the two most commonly used techniques [30-31]. The former calculates fields so as to cancel the reflection on the boundary, and the latter places absorbing materials (conductive medium) close to the boundary to suppress the reflection. In general, PML can provide orders-of-magnitude lower reflection than Mur's condition so that it is widely adopted by FDTD users [28]. In the following chapters, our FDTD simulation results are all based on the PML boundary condition.



Chapter 3

Band-Edge Slow Light Modes in Two-Dimensional Slab Photonic Crystal Waveguides

3.1 Introduction

Photonic crystal (PhC), consisting of periodically-varying dielectric materials, exhibits the ability to manipulate the propagation of light in both passive and active optical devices [23]. If properly designed in geometry, a photonic band gap (PBG), analogous to electron band gap in semiconductors, would be created [34-35]. It is believed that photons can be amenable controlled by introducing artificial defects into the ordered crystals [2, 36]. For example, point defects, where a single or a few periodic dielectric materials are removed, have been realized as cavities at nanometer scale [37-38].

The simplest type of photonic crystal consists of two alternative thin films with different refractive indexes [39]. This 1D photonic crystal, however, does not have the flexibility for being used in a complicated photonic circuit. A full-blown 3D crystal with a complete band gap, in which light at the frequency of defect states can be trapped or guided without losing any energy, would be a good candidate for the realization of omni-functional photonic chips [4, 40]. However, the complicated fabrication of 3D structures keeps them from being further applied. As for 2D crystals, they have many advantages, such as well in-plane light confinement and excellent integration with photonic and electronic devices. But the deficiency of vertical confinement would create another path for light to escape, resulting in serious energy

leakage.

Recently, 2D photonic crystal slab structures, where dielectric slab with planar photonic crystal patterns are sandwiched between two low dielectric constant materials, were proposed and studied extensively [10, 41]. Such structures not only maintain the superiority as 2D crystals, but also effectively confine light in the vertical direction by means of total internal refraction. If we could create high refractive index contrast in between the dielectric slabs and choose the adequate thickness of the sandwiched layer, a pseudo 3D PBG will be formed. One of the most accomplished structures that have been reported so far is that fabricated on silicon-on-insulator (SOI) substrate [42]. This structure consists of Si/SiO₂/Si (from surface layer to substrate) and has been maturely developed as the platform for ultra large scale integrated (ULSI) circuits in current semiconductor industry. Strictly speaking, Si is not a good candidate for photonic devices because of its natural characteristic of indirect band gap, but its superior properties, such as high refractive index ($n_{Si}=3.4$) and low absorption coefficient ($\alpha_n < 1 \text{ cm}^{-1}$, at $n_0=8 \times 10^{16} \text{ cm}^{-3}$ and $\lambda=1.55 \mu\text{m}$) meet the needs in optical communication network [43]. In addition, the low dielectric constant material of SiO₂ ($\epsilon_{SiO_2}=3.9$) can be easily removed with solution, buffered HF (BOE), thus turning SOI substrate into a membrane structure of air/Si/air/Si bulk. The suspended membrane hence possesses fairly large index contrast ($n_{Si}/n_{air}=3.4/1.0$) which can reinforce the confinement of light in a vertical direction. Moreover, the thickness of the membrane (Si layer of SOI) is always chosen to be half of the wavelength at which light transmits in the material to satisfy the lowest-order modes of standing waves. This is especially important for Si-based planar photonic crystal devices aimed at optical applications.

Examples of such most studied slab devices are 2D photonic crystal slab waveguides [44]. By inserting line defects into the periodically-arranged crystal

lattices, a certain frequency of light waves will be guided along the defect waveguides with less intensity loss because of the formation of defect modes in above-mentioned pseudo 3D PBG. Over the last decade, various applications of these waveguides, like photonic beam splitter [45], channel-drop filter [46], all-optical switch [47] and so on, were developed. Moreover, many interesting physical phenomena have been observed in such slab waveguides. One of them is “slow light” [20].

Slow light, as implied by the name, is that the speed of light wave is slowed down to the value much smaller than that in vacuum. It is expected that a great variety of applications, such as optical delay lines, buffer devices, and memory to store optical signals could be carried out if the light speed can be controlled at will. Since the photonic crystals are a category of band structure engineering, the slope of the corresponding dispersion curves, $d\omega/dk$, would determine the energy propagation velocity of light waves in the crystal patterns. Accordingly, it makes possible to retard the propagation speed of light waves if the photonic crystal patterns are designed properly. In the band diagram of photonic crystal slab waveguides, the defect bands are formed within the photonic band gap because of the introduction of line defects. Waveguide modes corresponding to the defect bands would propagate along the slab waveguide at different velocities if the shapes of the defect bands are not linear lines. Therefore, it is practicable to observe propagation light waves at extremely slow velocity in photonic crystal waveguides.

In the following, we start with slow light by taking 2D photonic crystal slab waveguides with single line defect (W1 type). First, the band diagrams of the waveguides were calculated by using plane wave expansion (PWE) method with effective index approximation. Next, we demonstrated the performance of the fabricated W1 type slab waveguides in experiments. After that, the deduced group velocities as a function of wavelength were obtained by means of frequency-domain

measurement (Fabry-Perot method) and time-domain measurement (phase-delay approach), respectively. Finally, the advantages and disadvantages of the two measurement methods will be showed and an improved way to measure the ultra slow light in photonic crystal waveguides will be proposed.

3.2 Band Diagram

Figure 3.1(a) is a pattern of 2D photonic crystal slab waveguide used in our calculations. A row of crystals is removed from the otherwise hexagonal lattices to form a so-called W1 type photonic crystal waveguide. The radius and the refractive index of crystals are assumed $r_0=0.255a$ and $n_{air}=1.0$, respectively. Si substrate was used as the material of the slab in simulation so as to meet the practical samples. The effect of the thickness of the slab was approximated by the approach of effective index of guided modes in the dielectric slab [48]. In this way, calculation dimension can be reduced from 3D to 2D without altering other simulated results, such as the field distribution of eigenmodes. A supercell was used as a primitive unit cell to construct the waveguide in spatial domain, as shown in Fig 3.1(b). And then, by using the PWE method, this supercell was applied to Maxwell equations (described in Chapter 2) to solve eigenmodes of 2D photonic crystal slab waveguides.

Figure 3.1(c) is the calculated band diagram for TE-like modes of a W1 type photonic crystal waveguide. The dash line, marked as light line, results from the air-cladding ($n_{air}=1.0$) and indicates a demarcation between the leaky mode region and photonic crystal slab mode region. Waveguide modes above this line are leaky. While the gray region shows the photonic crystal slab modes which can propagate inside the slab, the white area represents PBG where light transmission is forbidden.

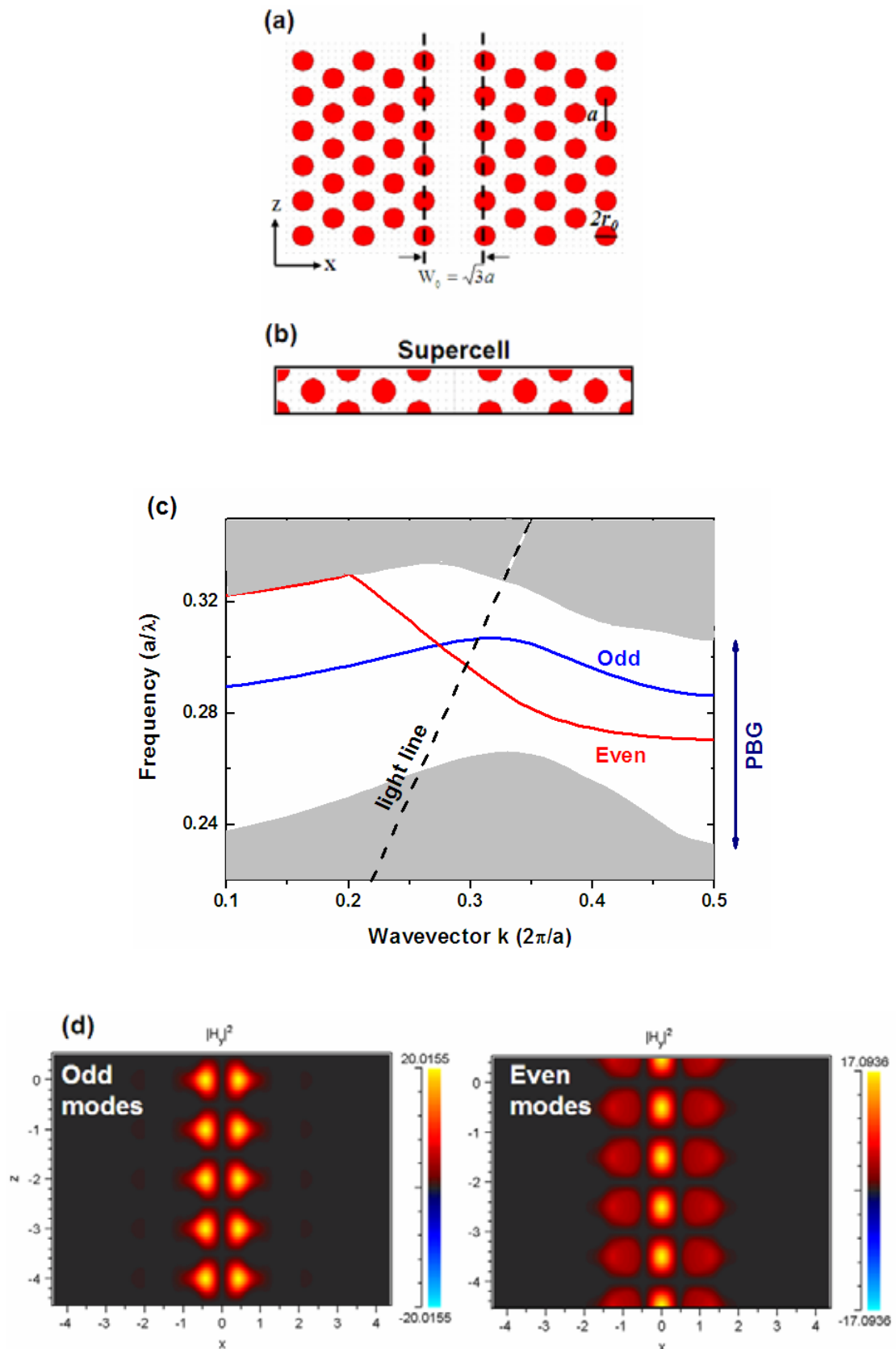


Fig. 3.1 (a) Schematic of a W1 type photonic crystal waveguide. (b) A selected 1×10 supercell. (c) Band diagram for TE-like modes of W1 type waveguides. (d) Y-components of magnetic field in the defect waveguide. (Left) Odd modes (Right) Even modes.

Of interest are the two unusual defect bands within the PBG. These two bands allow a certain frequency range of waveguide modes to propagate along photonic crystal line defects without leakage because of in-plane PBG confinement and TIR in the vertical direction. Close inspection of the field distributions of the guided modes in the two bands exhibits highly symmetry along the central axis of the defect waveguide, named odd and even modes (see Fig. 3.1(d)).

Furthermore, it clearly appears that the gradients of the two bands under the light line become flat, especially at the zone edge of the bands. This suggests that group velocities of the guided modes within the narrow bandwidth region would be very slow. In order to further understand, we will examine the properties of even bands for the fabricated 2D photonic crystal slab waveguides by using frequency-domain and time-domain measurements in the following section.



3.3 Device Fabrication and Characterization

Based on the theoretical results given in Section 3.1, a 4-inch SOI wafer with a $2\mu\text{m}$ buried oxide and a 205nm thin silicon guiding layer were used as a slab dielectric material. W1 type photonic crystal waveguides with triangle lattice constant of $a=432$ nm and hole radius of $r=110$ nm were patterned by E-beam lithography and transferred upon the Si guiding layer by ion couple plasma (ICP) dry etching. Then the underlying SiO_2 cladding layer was removed by selective wet etching using HF solution to form an Air/Si/Air membrane structure, as shown in Fig. 3.2. Si tapered ridge waveguides were connected to both sides of photonic crystal waveguides. W1 type slab waveguides with different lengths ($L=50\sim 3024\mu\text{m}$) were prepared for the following propagation loss measurements. The total lengths of all samples, including

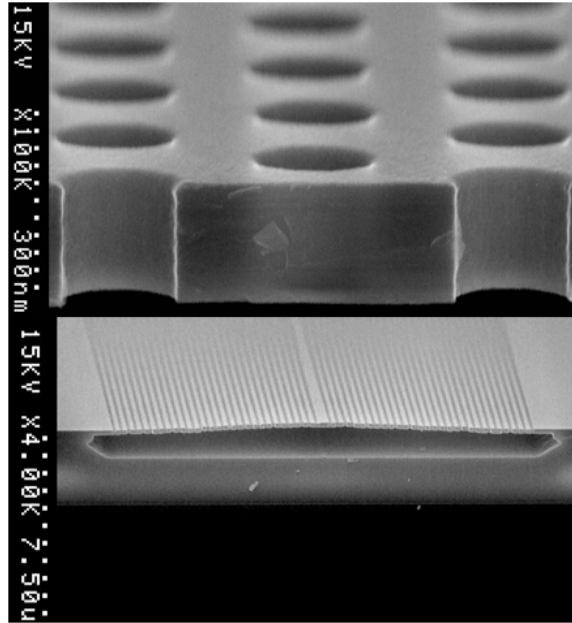


Fig. 3.2 SEM micrographs of the fabricated W1 type photonic crystal waveguides. The lattice constant and hole radius are 432nm and 110nm, respectively. The thickness of the slab is 205nm.

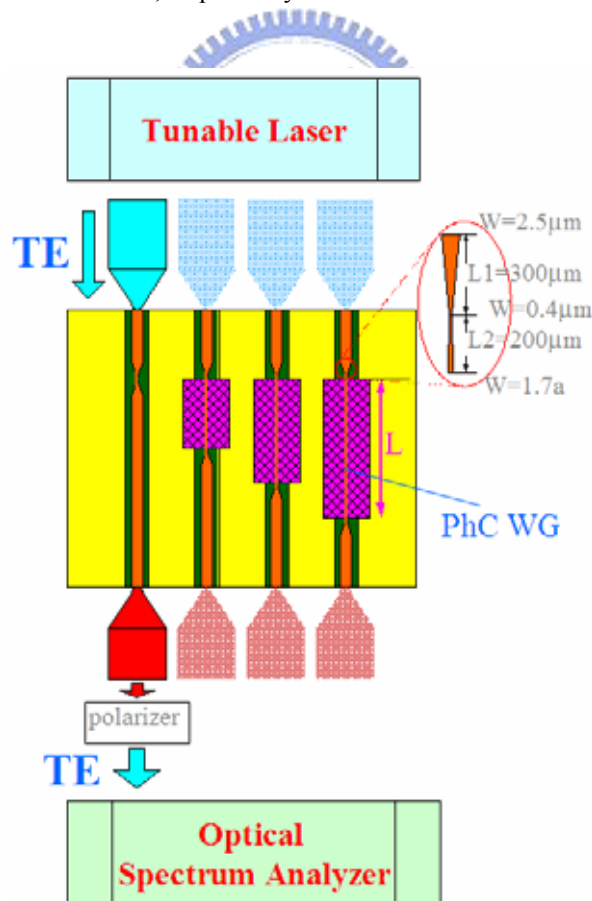


Fig. 3.3 Schematic illustration of the measurement system [49]. The inset shows the taper structure between Si and photonic crystal waveguides.

Si taper waveguides and photonic crystal waveguides, were fixed at 6mm.

Figure 3.3 shows the schematic of the measurement setup. A long-wavelength tunable laser with wide bandwidth of $\lambda=1490\sim 1620$ nm was used as light source. Linearly TE-polarized light ($E // \text{PhC plane}$) was coupled into the samples by using polarizers, single-mode optical fibers and objective lens. Light passing through photonic crystal waveguides was then analyzed by optical spectrum analyzer (OSA). A typical transmission spectrum of the fabricated W1 type photonic crystal waveguide with $54\mu\text{m}$ long is shown in Fig. 3.4. In this case, the structural parameters are

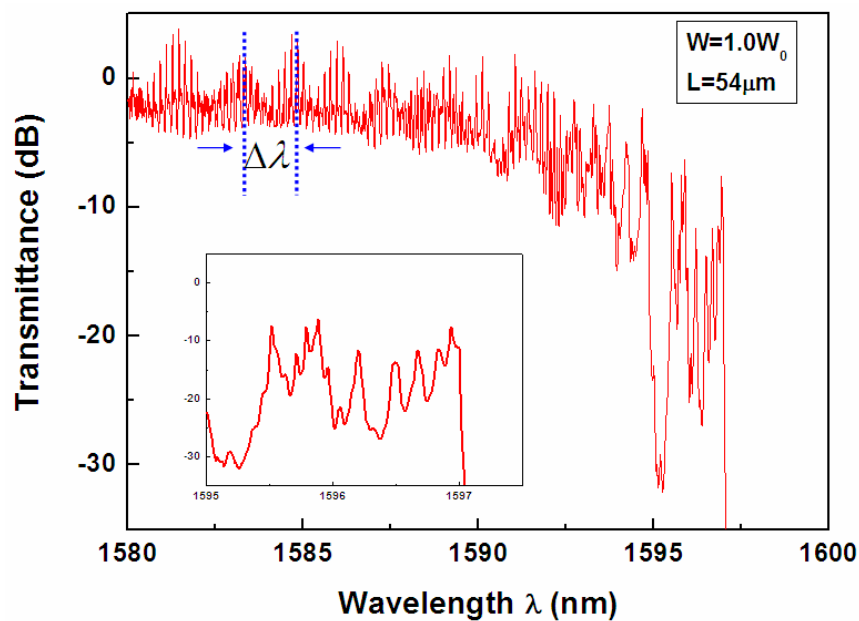


Fig. 3.4 Experimental transmission spectrum of a W1 type photonic crystal waveguide with a $54 \mu\text{m}$ length. The inset is the magnification of the cutoff region. $\Delta\lambda$ means the Fabry-Perot oscillation period.

designed to be the same as that in Fig. 3.1. The span from 1510nm to 1593nm corresponds to the bandwidth of the even modes calculated in Fig. 3.1. Similarly, other samples with different PhC waveguide lengths but the same structure parameters were also measured and shown in Fig. 3.5. Random dips observed in the

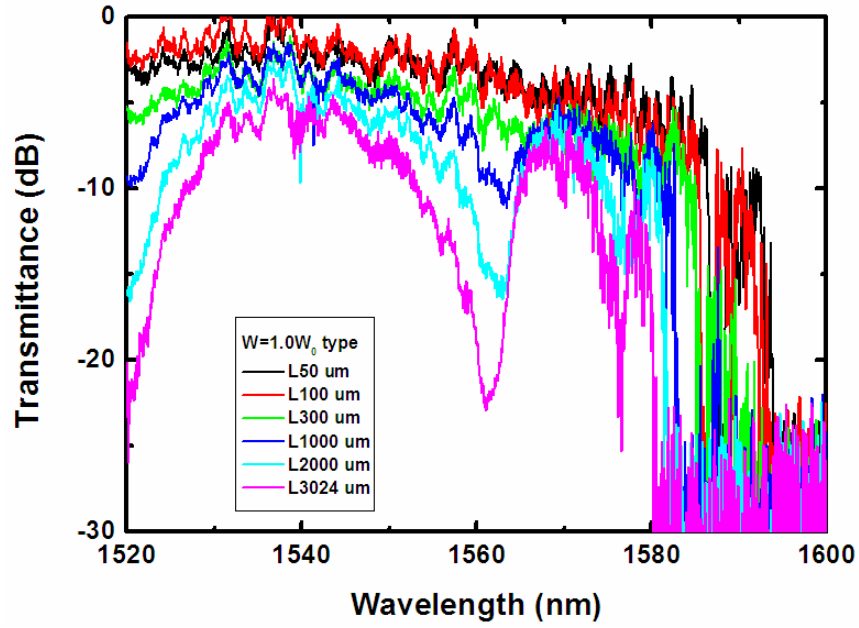


Fig. 3.5 Measured spectra of the samples with different waveguide lengths.

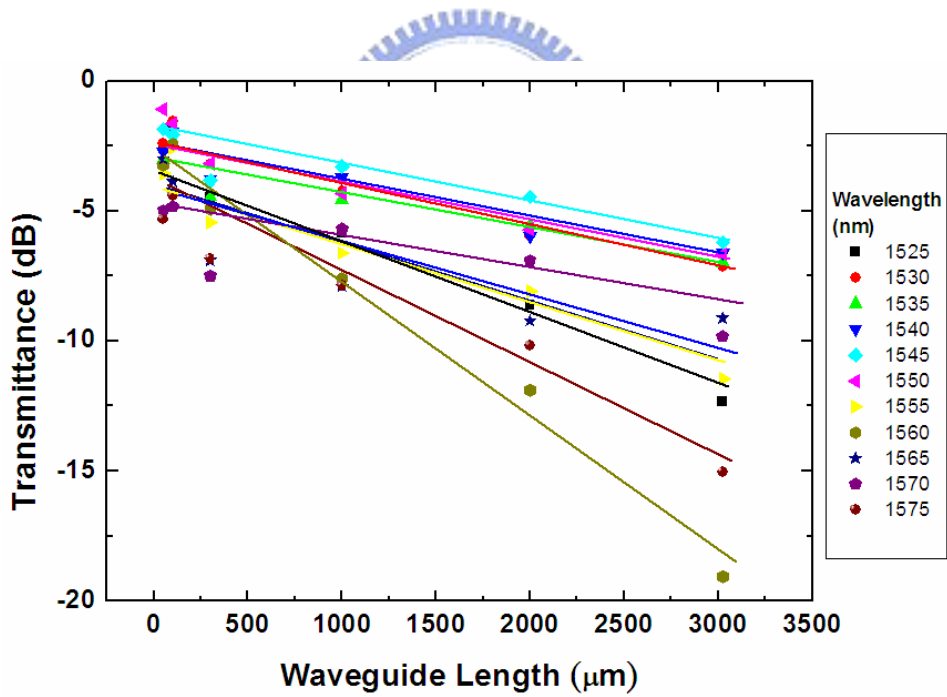


Fig. 3.6 Transmittance against photonic crystal waveguide lengths at different launch wavelengths.

spectra of longer waveguides are due to fabrication disorder, i.e. broken crystals. Different position of the cutoff in the curve results from the propagation loss of the waveguides, which is in proportion to waveguide length.

To estimate the propagation loss of the fabricated W1 type photonic crystal waveguides, the so-called “cut-back” method was used. The details of the method are described as follows. First, the original measured transmission curves were rearranged as a function of PhC waveguide length. Then, straight lines were applied to each modified curve by using the approach of least squares, shown in Fig. 3.6. Finally, the slopes of each fitting lines, presenting propagation loss, were plotted against the wavelength. Figure 3.7 shows the results of propagation loss measurements of the fabricated W1 type photonic crystal waveguides. It is clearly seen that the propagation loss in the range of 1530nm~1580nm is around 2~3dB/mm. In other words, if the device size is shrunk to 50 μ m, only 0.1~0.15 dB loss is shown. Such loss is too small to affect the normal operation of practical devices, hence our fabricated photonic crystal waveguides are considered ready to be applied to photonic integrated circuits. This value, to our knowledge, is the smallest one among those ever reported studies on photonic crystal waveguides.

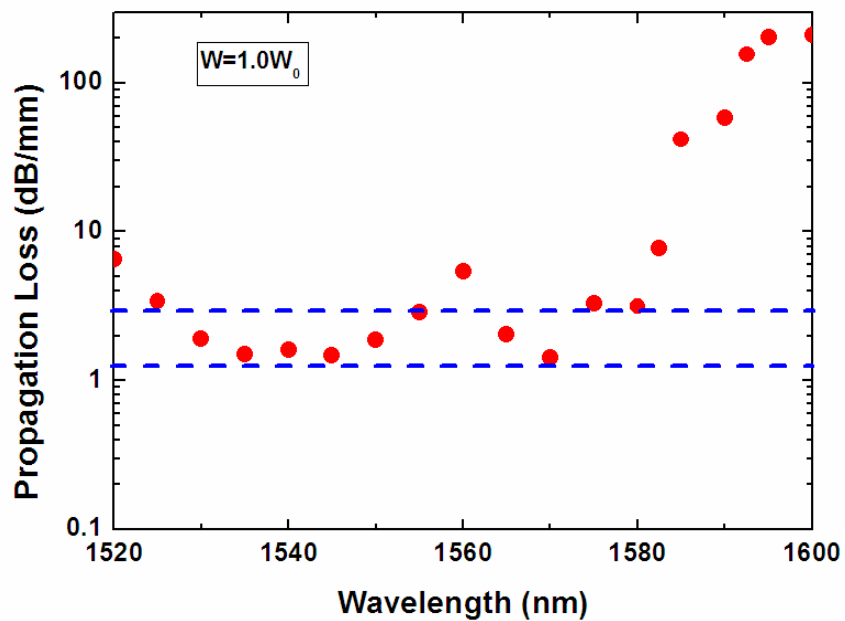


Fig. 3.7 Propagation loss spectrum for the fabricated W1 type photonic crystal waveguide. It is clearly that propagation loss is only 2~3dB/mm in the transmission region.

3.4 Group Velocity Measurement

3.4.1 Frequency-Domain Method

Since Si ridge waveguides were designed to connect with both sides of the photonic crystal waveguides (see the inset in Fig. 3.3), light reflection from the interface of Air and Si waveguide or Si and PhC waveguides resulted in the obvious Fabry-Parot (FP) interference patterns in spectra, as shown in Fig. 3.4. These FP patterns, however, exhibited abnormal oscillation periods ($\Delta\lambda$), which is getting smaller as wavelength increases. Based on FP formula, given by

$$\Delta\lambda = \frac{\lambda^2}{2Ln_g},$$

with λ being the FP resonant peak, L being the length of PhC waveguides, and n_g being the group index, a reduction of $\Delta\lambda$ implies the increase of n_g . Well-known in solid state physics, group index is defined as the ratio of light speed in vacuum to that in material, expressed as $n_g = c/v_g$ where c is the speed of light in vacuum and v_g is the group velocity. Therefore, a large value of n_g means that light wave propagates through materials at a small group velocity. Fig. 3.8 shows the deduced group indexes from Fig. 3.4 as a function of wavelength λ . The group index rapidly increases from 20 to 200 at around wavelength $\lambda=1592-1596\text{nm}$ and reaches its highest value $n_g=300$ at wavelength $\lambda=1597\text{nm}$ near the cutoff. This indicates a swift change of the energy propagation velocity of light in photonic crystal waveguides larger than that in air by a factor of 20-300.

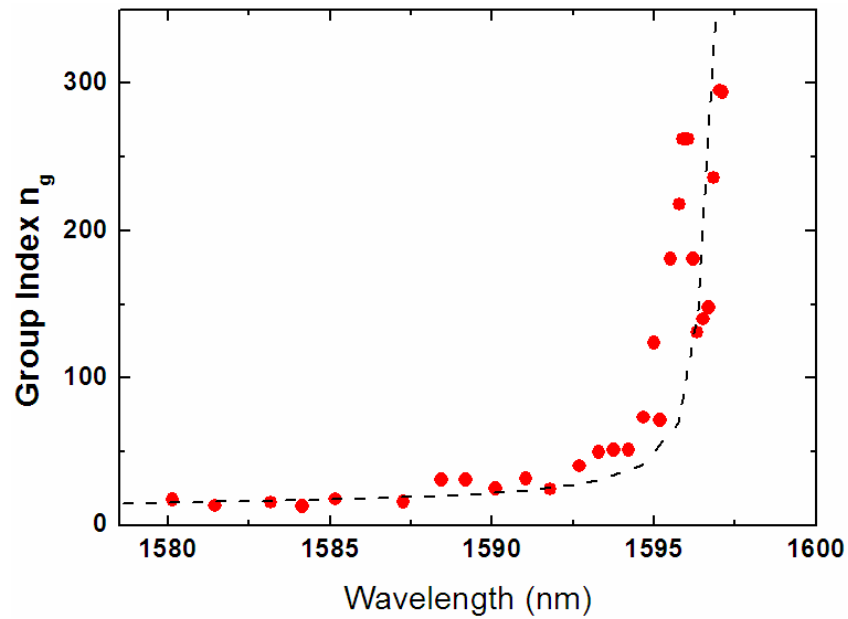


Fig. 3.8 Group index dispersion curve. The red dots show experimental n_g deduced from Fig. 3.4 by applying the Fabry-Perot formula. The dash line represents theoretical n_g , which is derived from the even mode band in Fig 3.1(c).

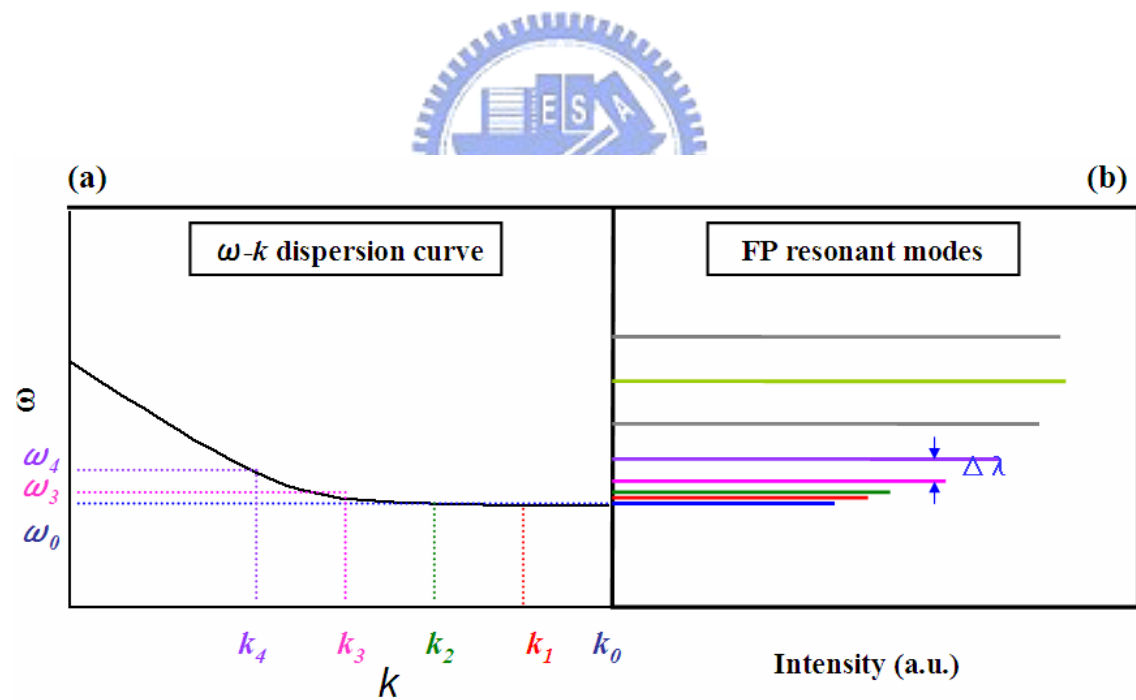


Fig. 3.9 (a) Magnified dispersion curve for the guided modes around the band-edge region. (b) Illustration of the Fabry-Perot resonant modes, which correspond to the guided modes in W1 type photonic crystal waveguides.

Since these group indexes were derived from the measured spectra by means of FP method, longer PhC waveguides would offer better opportunities to explore extremely large group indexes of light waves than short ones. This is because FP modes spacing is inversely in proportion to the waveguide length. The narrower the FP mode spacing, the more likely we are to approach the band edge points of guided modes. Figure 3.9(a) is a magnified dispersion curve around the band edge of even modes in W1 type slab waveguides. Figure 3.9(b) is a sketch of corresponding FP resonant modes in spectrum. Here, we assume that the dispersion curve is in parabolic shape and wave vector at the band edge of the first Brillouin zone is k_0 , which corresponds to a normalized frequency ω_0 . According to a parabolic approximation, we could express other normalized frequency ω around band edge as

$$\omega \approx \omega_0 + \left(\frac{\Delta k}{\alpha}\right)^2$$

where α is a numerical parameter related to hole radius, refractive index, and pattern structure, and Δk is the wave vector difference in dispersion curve, which is given by $\Delta k = |k_1 - k_0| = |k_2 - k_1| = |k_3 - k_2| = \dots$, and is in proportion to $1/L$. By differentiating the dispersion curve, group velocity is given by

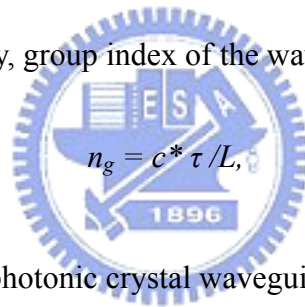
$$v_g = \frac{d\omega}{dk} \approx \frac{\Delta k}{\alpha^2} \approx \frac{(\omega - \omega_0)^{1/2}}{\alpha}.$$

As the waveguide length (L) increases, Δk would become smaller. So, it should be possible to achieve $v_g \approx 0$ at $\omega \approx \omega_0$ in theory. In practical experiments, however, a long waveguide would cause a large propagation loss. Therefore, we believe if the optimum waveguide length is found, an approximately ultimate band edge point of the guided mode, which corresponds to the extremely large group index, could be

observed.

3.4.2 Time-Domain Method

The other approach to determine velocity dispersion of photonic crystal waveguides is to monitor the phase delay of launched signal. Figure 3.10 is the schematic view of our time-domain measurement system. A 3G Hz(ω) modulated signal was steered into two branches: one is conducted to the fabricated photonic crystal waveguides and the other is directed to the phase combiner. Due to the different optical paths, the phase of the modulated signal passing through photonic crystal waveguides would differ from the original signal by an amount of $\Delta\Phi$. Since delay time is given by $\tau = \Delta\Phi/\omega$ where ω being the modulated frequency, group index of the waveguides can be determined via



$$n_g = c * \tau / L,$$

where L is the length of the photonic crystal waveguides.

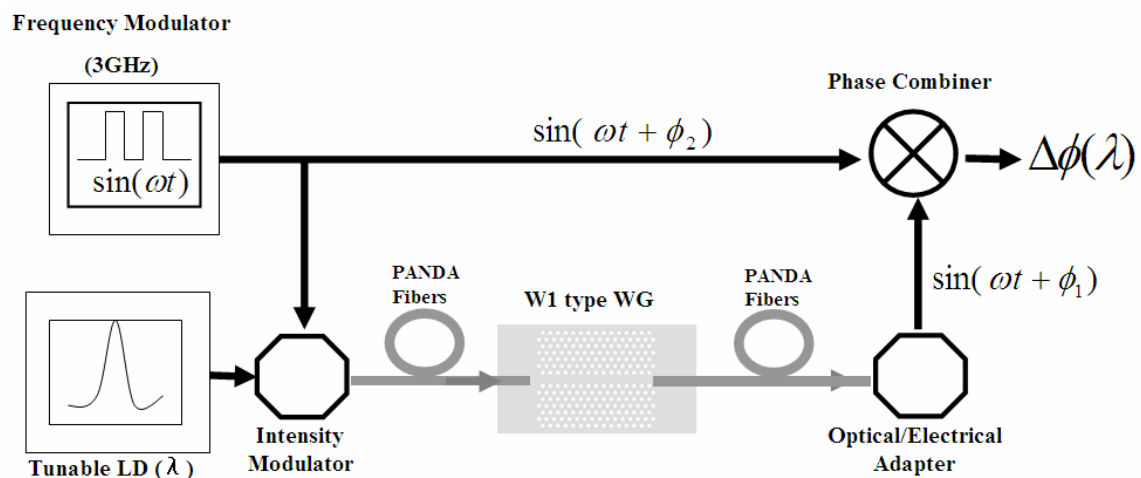


Fig. 3.10 Illustration of the phase-delay measurement setup.

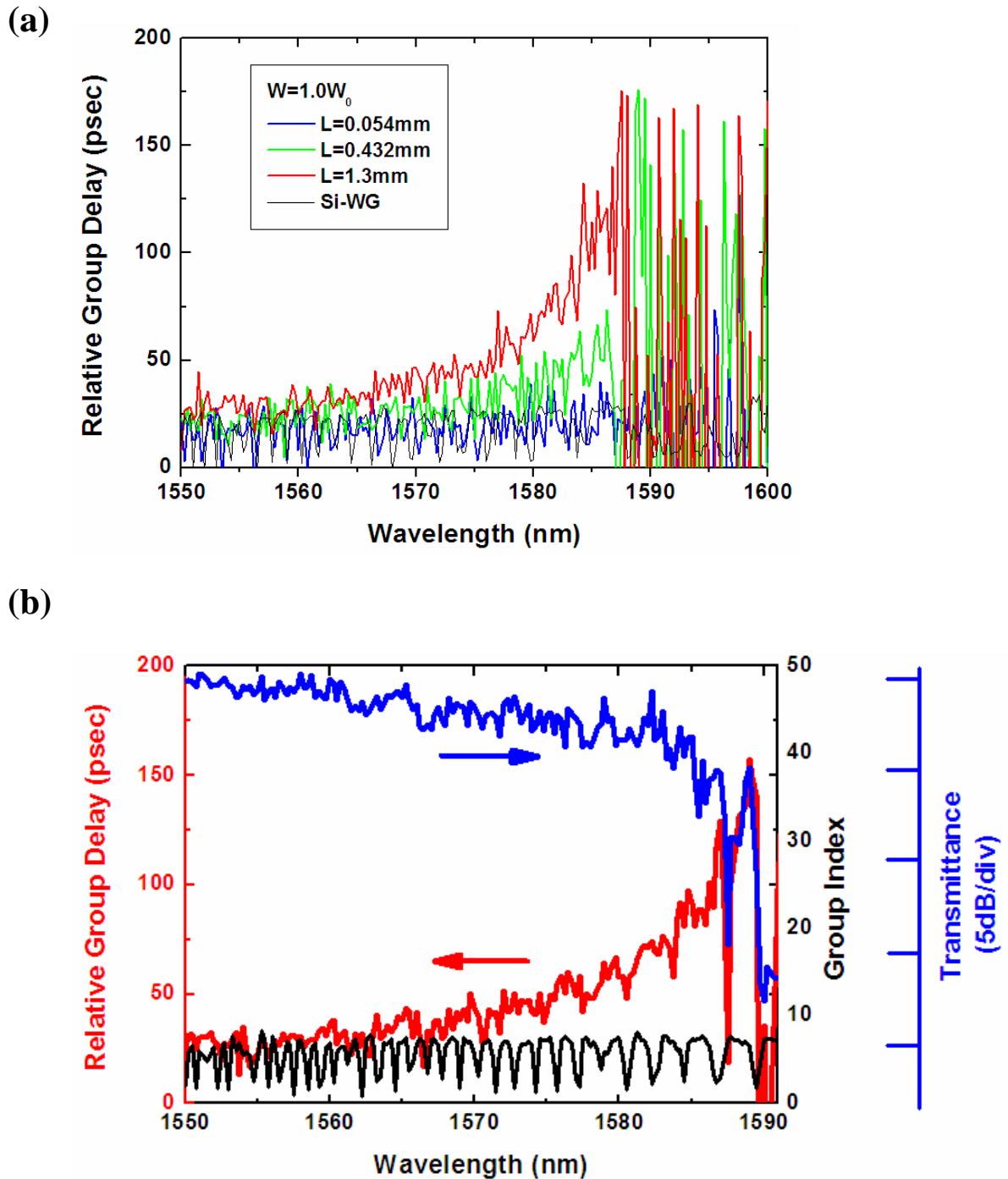


Fig. 3.11(a) Measured group delay time for the samples with different photonic crystal waveguide lengths. (b) Group index dispersion curve for the 1.3mm long W1 type photonic crystal waveguide. The black line in (a) and (b) represents the signal transmits over a Si waveguide.

Figure 3.11(a) shows the measured relative group delay time for W1 type photonic crystal waveguides with different lengths. Here, the structural parameters of all samples are designed to be the same as those in Fig. 3.1. The resolution of

time-domain scale is 0.1psec and the fluctuation shown in the plot comes from the internal FP noise of the waveguides. It clearly shows that the delay time rapidly increases at the cutoff region. However, due to the limited function of the modulator in our measurement system, the maximum deduced group index from the longest sample ($L=1.3\text{mm}$) is only 40 at around $\lambda=1590\text{ nm}$, as shown in Fig. 3.11(b). The information behind this point can not be analyzed. Compare this result with what we have obtained in frequency-domain measurement, the obtained group indexes are almost the same from $n_g=15$ at $\lambda =1580\text{ nm}$ to $n_g=40$ at $\lambda =1590\text{ nm}$. This again confirms that light waves at launched frequency close to the band-edge guided modes are rapidly retarded when passing through photonic crystal waveguides due to the unique characteristic of dispersion.



3.5 Discussion

While these two measurement methods provide convenient ways to examine the slow light phenomena in 2D slab photonic crystal waveguides, some disadvantages of the methods impede the further exploration of precise large group index. In frequency-domain measurement, for example, intrinsic FP noise, resulting from other FP cavities formed due to different interfaces of Air/ Si waveguide or Si/PhC waveguides, would couple into the measured signals of transmission spectra, thereby causing the wrong determination of group index. This circumstance usually occurs when we measure longer photonic crystal waveguides because of their corresponding dense and narrow FP oscillation periods. This is why short PhC waveguide length is usually chosen for frequency-domain measurements. However, if we attempt to approach the guided modes at the cutoff region (band edge of the first Brillouin zone),

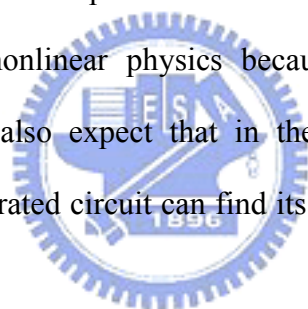
samples with long waveguide lengths are preferred (as mentioned in Section 3.4.1). Recently a novel approach, utilizing a Mach-Zehnder interferometer to acquire n_g , was proposed by IBM researchers to solve this contradiction [50]. They showed that a precise and large value of group index up to $n_g=300$ was successfully obtained even in a short ($L=50\mu\text{m}$) or a long ($L=250\mu\text{m}$) photonic crystal waveguide. The detail of this method will be introduced in Chapter 4.

As for the time-domain method used in this work, a major problem of observing extremely small group velocity v_g lies in propagation loss and dispersion of photonic crystal waveguides, which lead to the modulated signal weakened and distorted. This problem causes a vital failure in the detection of phase delay in the cutoff region, especially for those samples with longer PhC waveguide lengths, as shown in Fig. 3.11. Shortening the waveguide length would reduce propagation loss, yet it would result in the observed group delay time being too small to be analyzed precisely in the cutoff region. This is because low frequency of the modulator (3G Hz) was used in the experiments so that the resolution is not good enough. The tradeoff is to choose modulated frequency as high as possible to obtain the best temporal resolution (i.e., the highest number of oscillation per second). A good example can be found in [51]. The authors launched a 19 GHz small-modulated signal into a $20\mu\text{m}$ -long photonic waveguide and successfully obtained extremely high group index (>230) near the cutoff edge.

3.6 Summary

We have fabricated 2D slab of W1 type photonic crystal waveguides on SOI wafers. Very small propagation loss (2~3dB/mm) of the fabricated waveguides was

demonstrated by using the “cut-back” method. We also have reported on measurements and theoretical calculations of group indexes of light propagating in the W1 type slab waveguides near the cutoff region. Extremely large group indexes of 200~300 were observed from the measured spectra by the use of Fabry-Perot method. Results obtained from the time-domain measurement approach, which determines group velocities by detecting phase delay of a 3GHz-modulated signal passing through the waveguides, also showed large group indexes at position close to the band edge. In addition, the wavelength dependence of the group velocities deduced from the band diagram fit well with the measured data. These high values of group velocities indicated that light wave propagates through the photonic crystal waveguides at extremely slow speed. This characteristic would offer good opportunities of exploring nonlinear physics because of strong enhancement of light-matter interaction. We also expect that in the near future, photonic crystal waveguide as an optical integrated circuit can find its applications, like optical buffer devices.



Chapter 4

Inflection-Point Slow Light modes in Photonic Crystal Coupled Waveguides

4.1 Introduction

Since photon can be tailored at will in the man-made photonic crystal, utilizing photonic band gap structures to slow down the speed of light were recently acquiring much attention because of potential applications in devices such as optical delay lines [52-53], all-optical buffers [54-55], and optical storages [56]. One such promising structure is two-dimensional (2D) photonic crystal (PhC) slab waveguides [20]. As described in the Chapter 3, these waveguides, if designed properly, exhibit a unique dispersion relationship for the traveling light and can selectively retard the propagation speed of certain waveguide modes. Theoretical calculations have shown that extremely small group velocities can exist for the defect mode at the band edge of PhC waveguides due to a relatively flat band structure [20, 57]. Experimental measurements of slow light in PhC waveguides have also been reported. Some used the frequency-domain approach, which indirectly deduce the group index by analyzing the transmission spectrum using Fabry-Perot or interference methods [20, 50]. Some measured the phase delay of modulated signal to determine the group velocities [51, 58]. Results from direct time-domain measurements on the wave propagation in PhC waveguides, however, are very limited [59-60] because of the narrow operation bandwidth and large group-velocity-dispersion at the band edge.

Recently, Mori and Baba proposed a photonic crystal coupled waveguide

(PhCCW), where a unique flat band of coupled modes is formed in the photonic band gap [61]. An S-shaped dispersion curve with a flat region (or the inflection point) inside the first Brillouin zone was obtained for the waveguide mode. Their simulation results showed that the waveguide mode has a wider operation bandwidth and a lower dispersion for slow light propagation than that of a conventional single line-defect PhC waveguide. However, the experimental realization of PhCCWs and the light behavior at the unique flat band have not been reported.

In this chapter, we present for the first time the measured transmission spectrum of a properly designed PhCCW to verify the existence of the unique flat band. Next, we demonstrate the deduced group velocities as a function of wavelengths by using an interference approach, where the spectra of an integrated Mach-Zehnder interferometer (MZI) employing PhCCWs were measured, to further clarify the inflection-point slow light modes of this flat region. Finally, we report the time-domain observation of the retardation of propagation pulses in a 2D slab PhCCW by using a high speed oscilloscope. The group velocities of the optical pulses at different wavelengths were measured. An extremely small group velocity of $0.017c$ was obtained at the wavelength of $\lambda=1537.30$ nm, which is very close to the inflection-point slow light modes in the flat band.

4.2 Band Structures of Photonic Crystal Coupled Waveguides

A PhCCW consists of two W1 type waveguides, where a row of air-holes (W1) is removed from the otherwise hexagonal PhC lattices [62]. The two W1 waveguides are separated by three rows of air holes. The radius of the holes in the center row (r_c) and those besides the waveguides (r_1, r_2) and the position of the holes along the W1

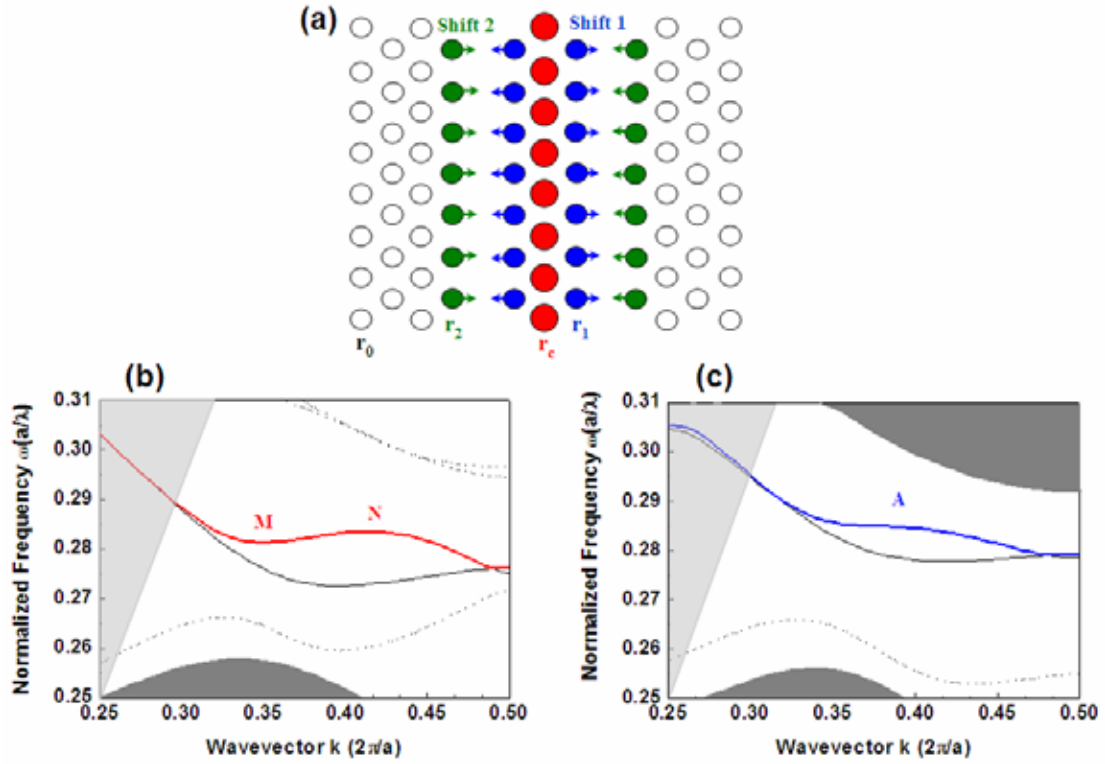


Fig. 4.1 (a) Illustration of PhCCWs. r_1 , r_2 , r_c , r_0 , shift 1, and shift 2 are all structural parameters. (b) and (c) are the calculated band diagrams of PhCCWs with different structural parameters, where black line and S-shape-like of blue (or red) line represent the odd and even modes of coupled bands in PhCCWs, respectively. The characters of A, M and N indicate the inflection points of bands.

Table 4.1 Structure parameters

Parameter:	r_0	r_c	r_1	r_2	Shift 1	Shift 2
(unit: a)						
Fig. 1.(b)	0.30	0.44	0.30	0.33	0.00	0.00
Fig. 1.(c)	0.28	0.41	0.26	0.27	0.00	0.22

waveguides (shift 1, shift 2) are used as design parameters, as shown in Fig. 4.1(a). By adjusting the structural parameters, we can easily obtain an S-shaped-like coupled defect band with clear inflection points. Figure 4.1(b) and 4.1(c) are the two examples of theoretical band structure for the guided modes, which were calculated by the 2D plane wave expansion method with effective index approximation. The corresponding

structural parameters are tabulated in Table 4.1. In Fig. 4.1(b), there are two inflection points, M and N, with a negatively sloped region in between. By optimizing the design parameters, we were able to obtain a nearly flat region between the two inflection points. In this case, with the band structure shown in Fig. 4.1(c), both the first derivative and the second derivative of the $\omega(k)$ curve approach zero at the inflection point A. So we have a situation that not only the group velocity of the waveguide mode is very small, but the dispersion of the propagating optical pulse is minimized.

4.3 Fabrication of Photonic Crystal Coupled Waveguides

Conventional 2D slab process for the PhC waveguides is carried out for this PhCCW fabrication. The detail is described in Chapter 3 and is also outlined here. A 4-inch SOI wafer with a 3 μm buried oxide layer and a thin silicon guiding layer (thickness = 205 nm) was chosen as a platform for fabrication. Devices were started by E-beam patterning of hexagonal arranged photonic crystals, whose lattice constant is designed as $a = 438\text{nm}$, followed by ICP-RIE dried etching. After obtaining air holes, the suspended silicon membrane was formed by removing the buried oxide layer using a selective wet etch, an HF solution. The top view of a completed coupled waveguide is shown in Fig. 4.2.

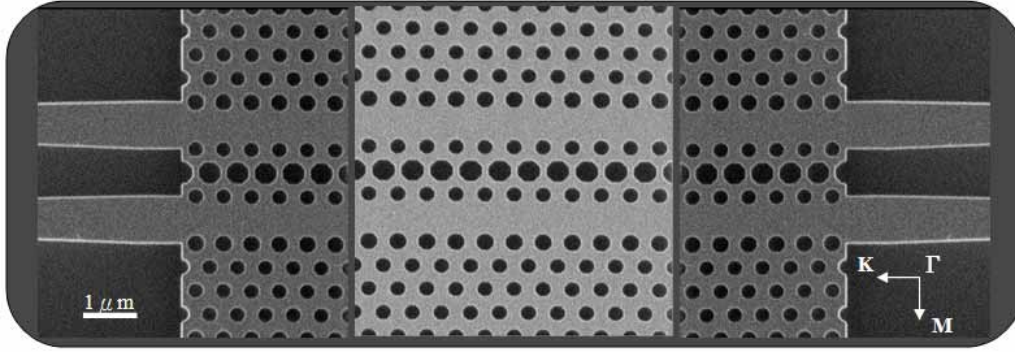


Fig. 4.2 SEM image of PhCCW with lattice constant $a = 438$ nm and hole diameter $2r_0=250$ nm. In this case, r_c , r_1 , r_2 , and Shift 2 is $0.44a$, $0.23a$, $0.30a$, and $0.15a$, respectively.

In order to investigate the characteristic of PhCCWs with such special defect bands in the experiments, some design rules are considered here. The input and the output of the PhCCW were integrated with two optical multimode interference (1x2 MMI) couplers for efficient coupling to the outside world (see Fig. 4.3). These MMI's, with 50/50 split ratio, allow us to excite and collect the coupled-defect modes at the input and the output ports of the PhCCW. Two kinds of the interface between the PhCCW and the access strip Si waveguides of the MMI's, named as Type I and Type II in Fig. 4.4, were fabricated to examine if or not the coupling efficiency is enhanced in the slow light region [63]. The width of the waveguides between the PhCCW and the MMI was tapered to ensure single mode propagation in the two branches. PhCCWs with three different lengths ($L = 100, 200$ and $500 \mu\text{m}$) were prepared.

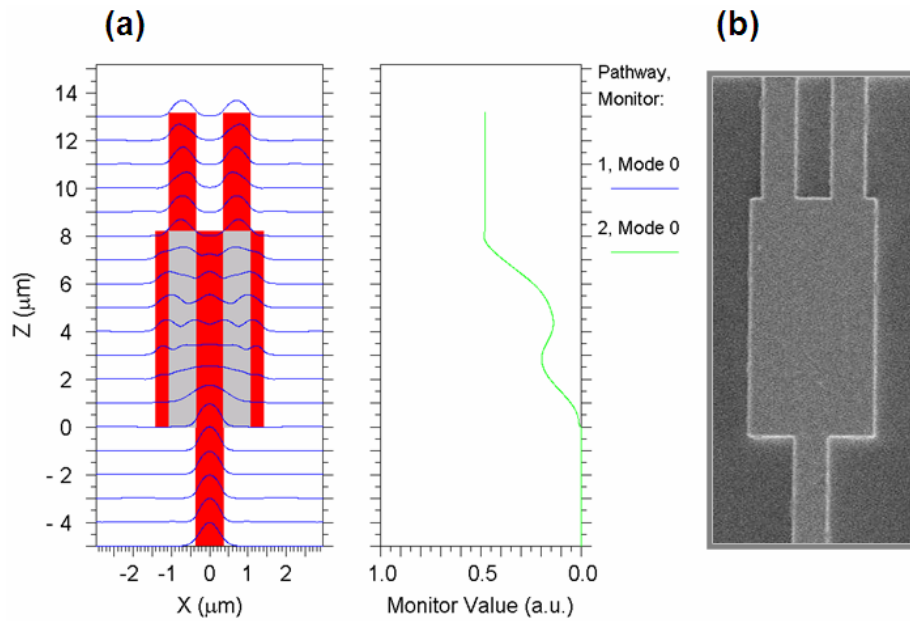


Fig. 4.3(a) A 1x2 MMI with 50/50 split ratio simulated by 2D beam propagation method. A Gaussian-shaped pulse at wavelength of $1.55 \mu\text{m}$ is used as light source in the simulation. (b) SEM micrograph of MMI device with dimension $3.2 \mu\text{m} \times 5.7 \mu\text{m}$ used in the experiments.

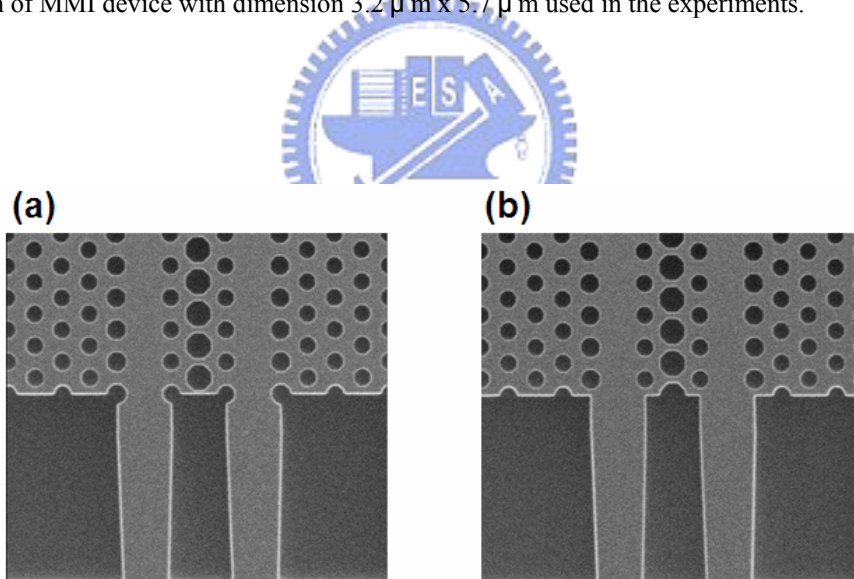


Fig. 4.4 Two kinds of interfaces. (a) Type I. (b) Type II.

4.4 Spectral-Domain Measurement

A typical transmission spectrum of the fabricated PhCCW with $200 \mu\text{m}$ long (Type II)

is shown in Fig. 4.5. In this case, the structural parameters were designed to be the same as that used in Fig. 4.1(c). A sharp dip (marked as point “A”) can be clearly seen at around $\lambda=1537$ nm indicating that the propagating light suffers a severe change in velocity. Usually for PhC waveguides, the so called “slow light” phenomenon is observed when waveguide modes propagate near the band edge [20]. But here, the dip (or slow light) is in the middle of the transmission spectrum. This is due to the special slow light region associated with the inflection point of the S-shaped-like dispersion relationship caused by the PhCCW.

In W1 type PhC waveguides, it has been demonstrated that different truncation at the interface of strip Si-PhC line defects would influence the coupling efficiency of the band-edge slow light modes [63]. This is explained by the photonic surface state at the coupling interface in resonance with the slow light modes. Here, the similar results were also observed in our fabricated PhCCWs. Fig. 4.6 (a) and (b) show the measured spectra, which correspond to the samples with truncations of Type I and Type II (see Fig. 4.4), respectively. It obviously exhibits that Type II has better

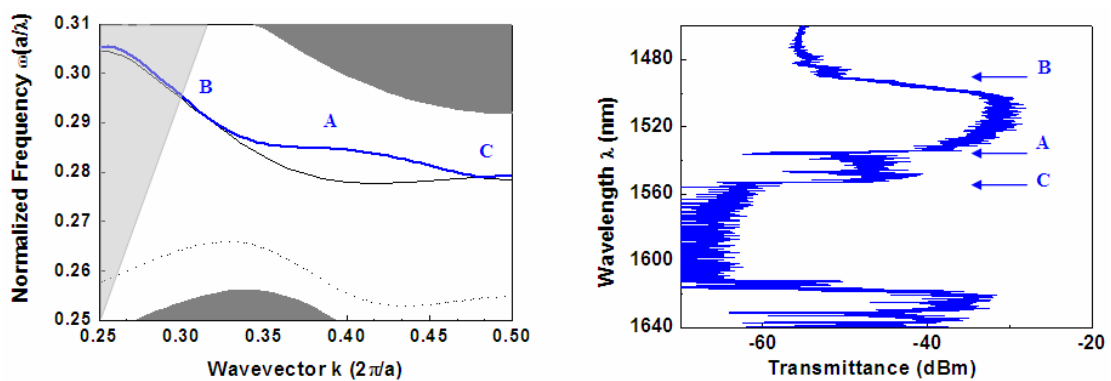


Fig. 4.5 (Right) Measured transmission spectrum of a PhCCW with length $L=200 \mu\text{m}$. In this sample, the structural parameters are designed to be the same as that used in Fig. 4.1(c). (Left) For convenience of comparison, Fig. 4.1(c) is placed here again.

coupling efficiency than Type I in the slow light regime by a factor of 5~7dB. This is also ascribed to the mode match of surface state (Γ -M) and line-defect state (Γ -K). So, it again confirms the importance of truncation design of the coupling interface as we explore extremely slow modes in PhC waveguides. In the following discussions, only samples with Type II interface are concerned.

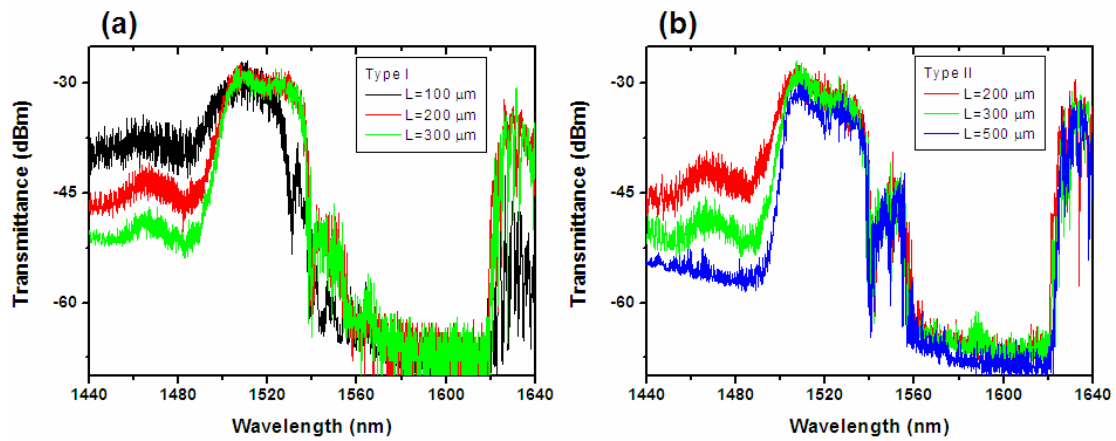


Fig. 4.6 Measured spectra for (a) Type I, and (b) Type II. It is clear that Type II shows higher transmittance at the cutoff than Type I.

For further clarification of the S-shaped-like band in PhCCWs, we also investigated the spectral dependence of the group velocities by utilizing interference method. Fig. 4.7(a) shows the schematic of the device layout. An integrated MZI structure [50], which consisted of a reference branch (stripe Si waveguide) and a signal branch (PhCCW butt-connected to MMIs), was used. Two MMI splitters that split light equally between the branches were applied to realize the interference experiments. The structural parameters of PhCCW were designed with the band structure shown in Fig. 4.1(c).

A typical transmission spectrum of this MZI device is shown in Fig. 4.7(b). The maximum and minimum of the oscillating fringes correspond to the constructive and destructive interference, respectively. It is seen very clearly that the oscillation period

changes rapidly between wavelengths of 1530 nm and 1540 nm. This indicates a sharp increase of the relative phase shift in interference. The group index of the propagating light in the PhCCW can be deduced from this interference spectrum using

$$n_g^{sig}(\lambda) = \frac{\lambda_{min} * \lambda_{max}}{2L(\lambda_{min} - \lambda_{max})} + n_{si}(\lambda)$$

where $L=200 \mu\text{m}$ is the length of a PhCCW and $n_{si}(\lambda)=3.4$ is the index of Si waveguide in the reference branch [50]. Figure 4.7(c) shows the deduced group index as a function of wavelength. We can see that the group index n_g increases rapidly as the wavelength increases above 1535 nm and reaches the highest value at around 1537 nm, and then diminishes beyond 1540 nm. For comparison, we have also calculated the group index from the S-shaped-like band structure shown in Fig. 4.1(c) using $n_g = c/(d\omega/dk)$. The result is shown by the black dashed curve in Fig. 4.7(c). Very good agreement was obtained between the measured and the calculated results, demonstrating the existence of small group velocities at around $\lambda=1537 \text{ nm}$, which corresponds to the inflection point, "A", shown in Fig. 4.1(c) and the dip shown in Fig. 4.5.

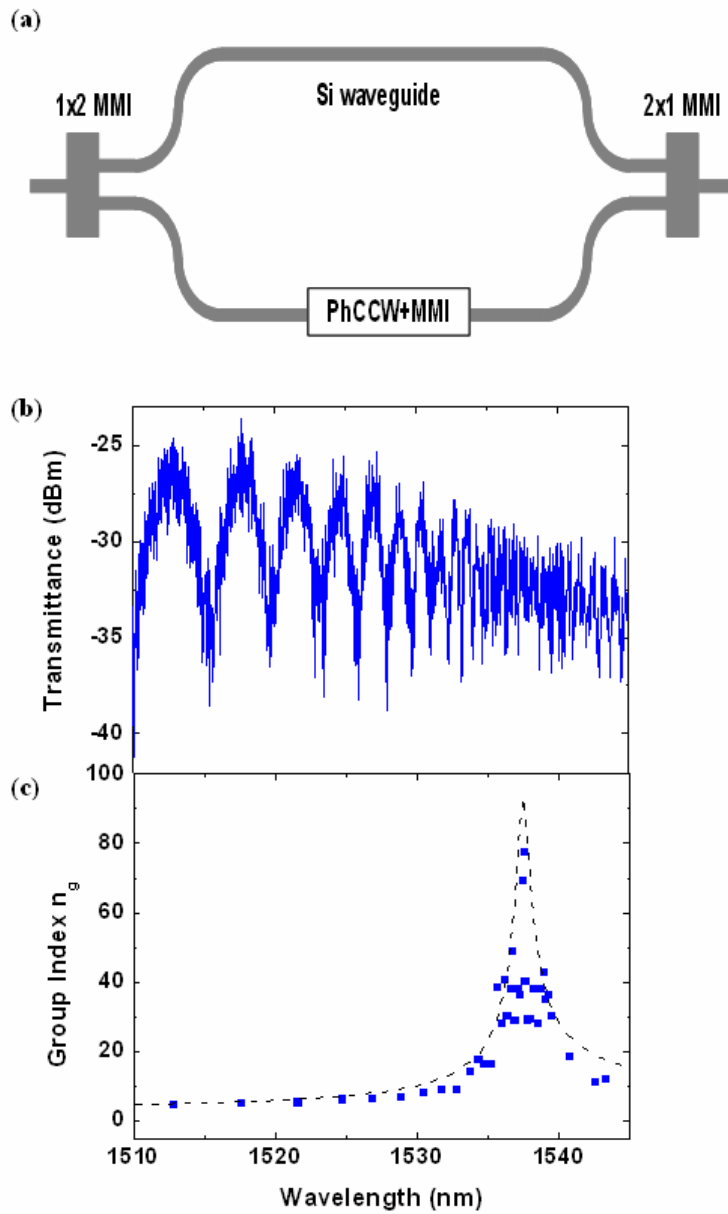


Fig. 4.7 (a) Schematic of an integrated MZI structure. The gray bold line represents the stripe Si waveguides. (b) Measured transmission spectrum of a MZI sample. In this case, the length and the lattice constant of PhCCW are $200 \mu\text{m}$ and 438 nm , respectively. (c) Wavelength dependence of group indices (blue squares) deduced from (b) by using inference approach. The black dash line shows the theoretical group indices calculated from the inverse of slopes of the blue line (coupled band) in Fig. 4.1(c).

4.5 Time-Domain Measurement

Next, we explore the temporal dynamics of the propagating light in this special slow

light region by doing the time-resolved measurements on the PhCCWs. Figure 4.8 shows the schematic of our time-domain measurement system. A passive mode-locked Er-doped fiber ring laser, operated in the 1525-1565 nm, was used as the light source. The repetition frequency of the pulses was 10 MHz, which corresponds to a period between pulses of 100ns. The light from the laser was amplified by an Er-doped fiber amplifier (EDFA) and then modulated by an optical tunable filter of bandwidth 0.244 nm. As a result, high power input pulses with a long pulse length of 24-28 ps (FWHM) were obtained. By utilizing a 1 x 2 fiber optic splitter module with a splitting ratio 90/10, 90% of the input power was steered into the sample under test and 10% goes into a tunable optical delay line. Another Tee type (2 x 1) fiber optic coupler with a coupling ratio 50/50 was used at the output to combine the two split beams into one. The output light collected was then amplified by a 2nd EDFA. The waveforms of the amplified pulses were finally displayed and recorded by an oscilloscope with a fast integrated optical-module, which has 28 GHz of unfiltered optical bandwidth for optical signal detection. To suppress the amplified spontaneous emission (ASE) from the EDFA, another optical tunable filter of bandwidth =0.6 nm was used between the 2nd EDFA and the oscilloscope.

In order to determine the group velocity of the waveguide mode, we used PhCCWs with three different lengths ($L=100, 200, \text{ and } 500 \mu\text{m}$). Since the optical delay line was the same for all three samples, the transmitted pulse from the delay line was used as a reference and the waveforms measured from samples with different lengths could be overlapped to show the propagation delay in the PhCCWs. Figure 4.9(a)-(c) show the transmitted pulses through the PhCCWs and the optical delay line

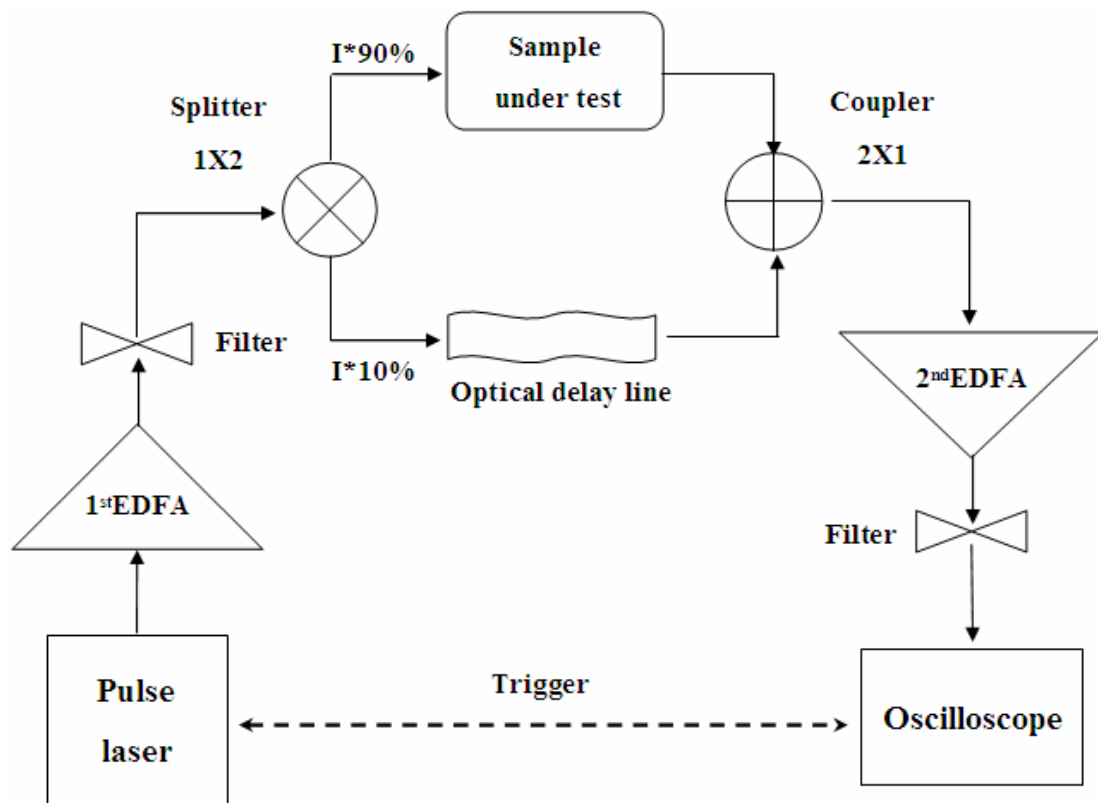
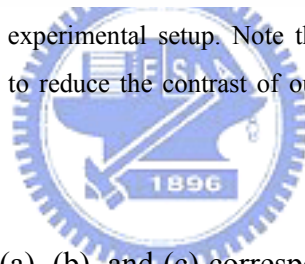


Fig. 4.8 Schematic diagram of the experimental setup. Note that a 1 x 2 splitter with uneven split percentage (90% and 10%) is used to reduce the contrast of output power between samples and the optical delay line.



recorded on the oscilloscope. (a), (b), and (c) correspond to measurements with input pulses of three different wavelengths $\lambda = 1541.02$ nm, 1539.38 nm and 1537.30 nm, respectively. The reference signal is the left most pulse in each figure and other pulses are measured waveforms of the transmitted light from the three samples. By measuring the delays of the output pulses with respect to the reference signal, the group velocity was then determined. Take Fig. 4.9(b) as an example, the duration time between the output pulses and the reference pulse was 99, 108, and 132 ps for samples with length $L = 100, 200$ and 500 μm , respectively. Plotting the duration time versus the waveguide length and fitting the data with a linear line (see Fig. 4.9(d)), we obtained a group velocity of $0.039c$. Similarly, the group velocity determined from the curves in Fig. 4.9(a), where the input pulse has a center wavelength of 1541.02 nm, is

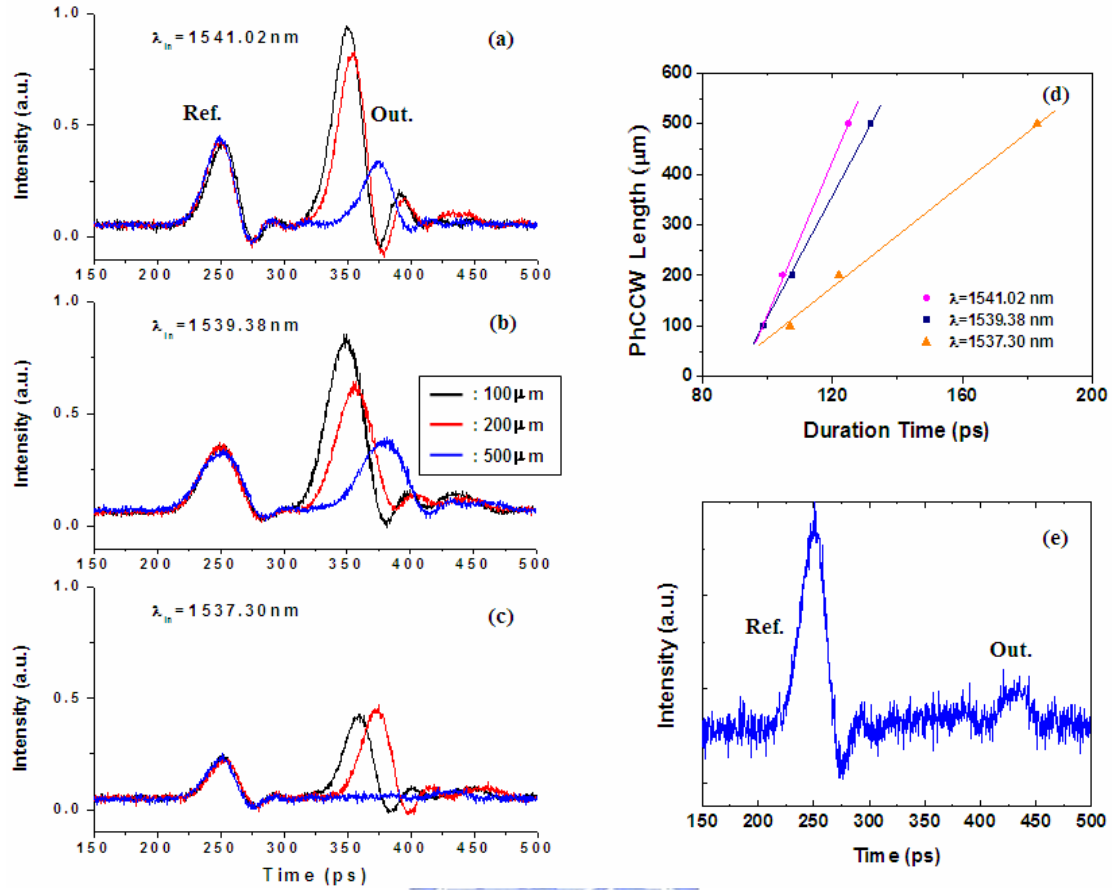


Fig. 4.9 Time-resolved measurements obtained by recording output pulses on the oscilloscope. The black, red, and blue lines represent samples with PhCCW length of $L=100$, 200 , and $500 \mu\text{m}$, respectively. The waveforms in the leftmost of plots, named reference signals (Ref.). Others correspond to output signals (Out.), which means pulses travel through PhCCW. Measurements at different central wavelengths of launched pulses $\lambda_{in}=1541.02 \text{ nm}$, 1539.38 nm , and 1537.30 nm are shown in (a), (b), and (c), respectively. The magnified plot of the blue line in (c) is shown in (e). A weak output signal is clearly observed. (d) The measured duration time with different launched wavelengths as a function of PhCCW length.

0.050c. The series of small damped oscillations following the output signals are thought to be from the signal reflected at the interface of Si-stripe and PhCCW and are not taken into consideration here.

In Fig. 4.9(c), where the input pulses have a center wavelength of 1537.3 nm , the pulses obviously travel slower than those in the other two cases. But the output waveform for the sample with $L=500$ is very weak (at $t=430\text{ps}$). This makes the determination of V_g difficult. For clarity, the blue line in Fig. 4.9(c) is magnified, as

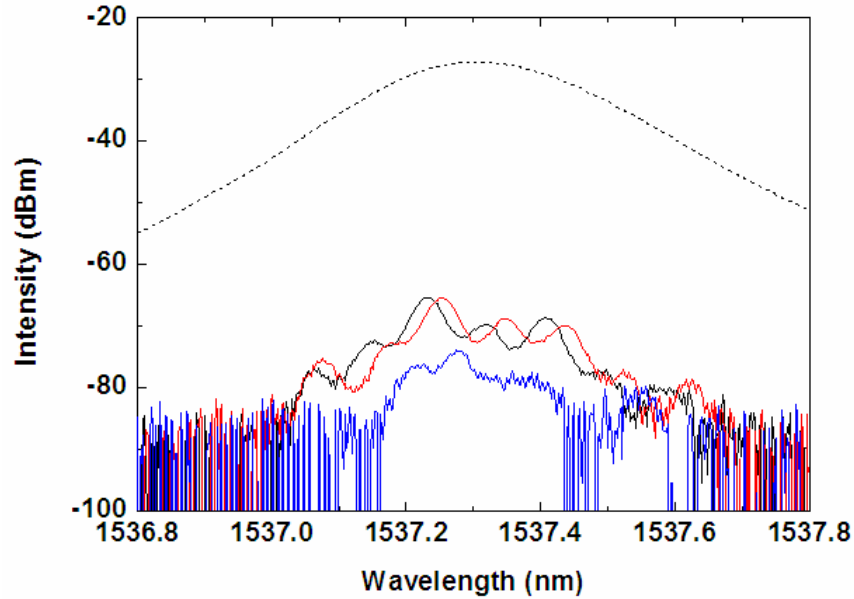


Fig. 4.10 Transmission spectra of input pulse (dotted line) and measured output signals (black, red, and blue lines) in Fig. 4.9(c).

shown in Fig. 4.9(e). Now a clear but weak output waveform can be seen.

To ascertain where this waveform originates from, spectrums of all output pulses in Fig. 4.9(c) were measured, as shown in Fig. 4.10. In this plot, the dotted curve represents the spectrum of the input pulse, which is centered at $\lambda = 1537.3$ nm and has a linewidth (-3dB) of $\Delta\lambda = 0.244$ nm. The black, red, and blue lines correspond to the measured spectra of output pulses traveling through PhCCW with length of $L = 100, 200,$ and $500 \mu\text{m}$, respectively. Because an optical filter is used for suppression the ASE, only a span of 0.6 nm of all output spectra is visible. The periodic ripples in the output spectra are due to Fabry-Perot noise, which originate from an intrinsic Fabry-Perot cavity formed by both facets of the samples. Besides being weaker, the output spectrum (blue line) for pulses of the sample with $L = 500 \mu\text{m}$ is distorted compared with those from the samples with $L = 100 \mu\text{m}$ and $200 \mu\text{m}$. This phenomenon can be explained by the group-velocity-dispersion (GVD) of PhCCW. As we approach the saddle point (or slow light) of the dispersion curve of the waveguide mode (see Fig. 4.1(c)), GVD is expected to become stronger. As a

result, after propagating through a long distance, the spectrum is slightly distorted. But from the spectra of the output waveforms, we are sure that the pulses measured, including the weak one after 500 μm , are all from the pulses launched at the input. From the delay times measured in Fig. 4.9(c), we determined, at $\lambda = 1537.30\text{nm}$, a very slow group velocity of only $0.017c$. In other word, the speed of light is slowed down by about sixty times than that in vacuum.

Using the same method, we have investigated the frequency dependence of group velocity in the wavelength range from 1545.00nm to 1537.30nm and compared it with the theoretically calculated group velocities obtained from the slopes ($d\omega/dk$) of the band structure in Fig. 4.1(c). The result is shown in Fig. 4.11(a). The deviation between the measured points and the theoretical curve is due to fabrication disorder, which results in slight difference in structural parameters. In spite of this discrepancy, it clearly shows that the group velocity goes down as the launched frequency approaches the inflection-point “A”. These extremely small group velocities are attributed to a relatively flat region in the band structure of the coupled waveguide modes. The slow light region is in the middle of the transmission spectrum of the waveguide mode. This is different from the previously reported slow light experiments in single line-defect photonic crystal waveguides, where the waveguide modes propagate near the zone edge (or the edge of the transmission spectrum) of the band structure. This gives us a larger tolerance in obtaining the slow light region.

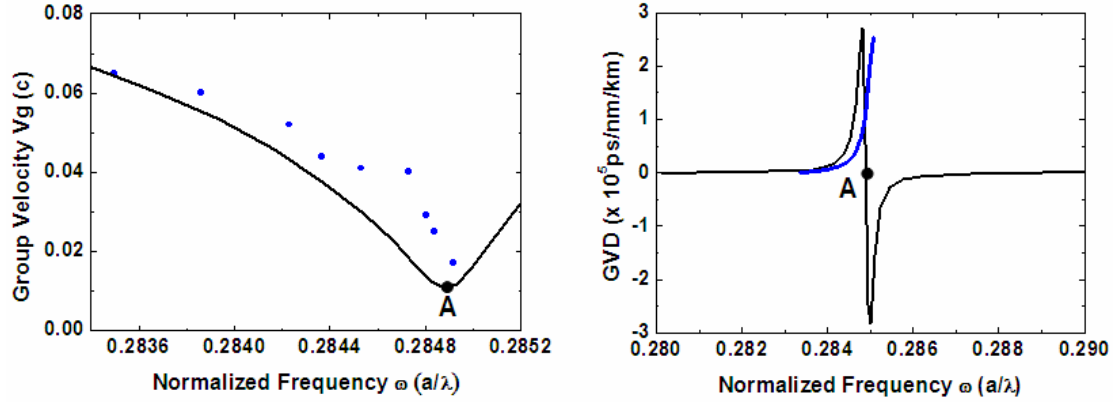


Fig. 4.11 (a) Measured group velocities (blue dot) in comparison with theoretical ones (black line), which are derived from the calculated band diagrams in Fig. 4.1(c). The character “A” indicates the calculated inflection point of the coupled band. The lowest group velocity in experiments is about $0.017c$ at $\omega=0.2849$ (or $\lambda=1537.30$ nm). (b) Calculated GVD (black line) from Fig. 4.1(c) and experimental GVD (blue line) derived from measured V_g in Fig. 4.11(a).

From the curve shown in Fig. 4.11(a), we can evaluate the value of group velocity dispersion (GVD) defined as $-(dv_g^{-1}/d\omega)$. Figure 4.11(b) shows the calculated GVD (black line) and the experimentally obtained GVD (blue line), which is obtained after curve fitting the data points in Fig. 4.11(a). Despite the offset in frequency in Fig. 4.11(b), the good qualitative agreement between the two lines indicates that the value of GVD ranges from 2×10^3 ps/nm/km at $\omega=0.2835$ to 2.5×10^5 ps/nm/km at $\omega=0.2849$. The observed GVDs are almost 3~5 orders of magnitude larger than those in a conventional single-mode optical fiber (typically 17 ps/nm/km at 1550nm), but 1~2 orders smaller than those in W1 type PhC waveguides. Moreover, different from those of the W1 type PhC waveguides [59-60], the calculated dispersion curve has a positive and a negative part, and in a very narrow region in between it goes to zero. Therefore, it is possible that by reaching the center point, A, one may obtain an extremely small group velocity with zero dispersion. Due to the narrow bandwidth of this reduced GVD region in the current design and the limitation of the measurement system, however, we did not succeed in exploring such reduced GVD region in the experiment. We believe that by further optimizing the PhCCW

structure to enlarge the bandwidth of the low dispersion region [61] or by launching a longer pulse length, it is possible to observe that the guided modes propagate along the PhCCW at an extremely group velocity and minimized dispersion.

4.6 Summary

We have designed and fabricated a photonic crystal coupled waveguide, where the guided mode has a unique flat band region within its photonic band gap allowing slow light propagation. Special inflection-point slow light modes that appear in the middle of the transmission spectrum instead of at the band edge were obtained. A sharp dip in the transmission spectrum and the peaking of the group index from the Mach-Zehnder interference measurement clearly indicate the existence of such inflection point. The group velocities of the optical pulses in this special waveguide were measured in time domain by comparing the propagation delay of the optical pulse through the waveguide with that of a reference optical delay line. A very clear slowdown of the optical pulses was directly recorded on a fast oscilloscope. An extremely small group velocity of $0.017c$ has been observed at $\lambda=1537.30$ nm, due to the inflection-point slow light modes. This study, to our knowledge, is also the first consistent and reliable observation of the inflection-point slow light in the spectral and time-domain analysis.

Chapter 5

Electrically-Driven Integrated Photonic Crystal

Nanocavity Coupled Surface Emitting Lasers

5.1 Introduction

In the last decade, utilizing the line defects to form the functional photonic crystal waveguides has been extensively studied and applied in the field of physics and engineering, as discussed in Chapter 3 and Chapter 4. In parallel with these studies, the point defects leading to the photonic crystal (PhC) nanocavities were also greatly developed [2, 10, 18-19, 64-65]. Defects or vacancies in photonic crystal are natural high Q resonators that can trap light and serve as laser cavities. It is also expected that the spontaneous emission rate in such tiny nanocavities can be altered in proportion to the cavity Q value and light localization; this is known as Purcell effect [66]. In addition, the potential of ultra high quality factor and extremely low mode volume makes photonic crystal nanocavities the most promising candidates for the experiments on cavity quantum electrodynamics (Cavity QED) [67-69]. The first successful experiment on point-defect laser was demonstrated by a Caltech group in 1999 [10]. They fabricated two dimensional (2D) slab photonic crystal nanocavities on an InP-based wafer, which has four pairs of InGaAsP quantum wells as light media, and observed pulse lasing action at a substrate temperature of 143K by optical pumping. At that time, a small mode volume (V) was $0.03 \mu\text{m}^3$, but a very low Q value of only 250 was obtained. In 2003, Y. Akahane et al. identified that due to the edge effect, the smaller cavities would result in more serious leakage, thereby drastically decreasing Q value [64]. They instead developed a so-called L3 nanocavity,

where three adjoining points were removed and the positions of the innermost two points were modified, and carried out a high Q cavity with $V=0.07\mu\text{m}^3$ and $Q=45,000$ by using a Si-based 2D photonic crystal slab. In 2005, B. S. Song et al. further achieved an ultimately high Q cavities ($Q=600,000$) using double-heterostructure, where the cavities were formed in between two W1 type PhC waveguides with slightly different lattice constants [18]. Based on this concept, NTT researchers pushed Q-value up to one million by inventing width-modulated-waveguide cavities in 2006 [19]. Their latest study showed these ultra high Q cavities could trap and delay photon at nearly 1ns [65]. On the other hand, since the resonant wavelengths of the cavities can be easily tailored to selectively pick up signals with specific wavelengths, nanocavities combined with photonic crystal waveguides, which function as photonic integrated circuits (like optical switches, channel add/drop filters, and optical inverters), have also been extensively proposed [70-72]. Moreover, the cavities with embedded quantum dots being on-demand single photon light source were implemented as well [73-75]. However, the above-mentioned work was all based on either optical pumping or light coupling from a passive waveguide and an external light source. Very few electrical pumping photonic crystal nanocavity lasers were reported because of the difficulty in device fabrication [76].

In this chapter, we demonstrate an integrated laser-nanocavity structure, where the laser light is directly coupled to the photonic crystal nanocavities. Since the laser light is generated by a lateral cavity similar to a conventional edge-emitting laser, electrical pumping is easily achieved like a regular laser diode. A two-dimensional photonic crystal slab with point defects, which were created as nanocavities, was used as a reflective mirror for the in-plane laser light, while the nanocavities served as couplers for light trapping and emission. Under the electrically-driven pulse operation, the characteristics of the strongly coupled surface emitting laser light from the

nanocavities were analyzed. Temperature dependence of the laser emission from the nanocavity was also measured. In addition, two side by side nanocavities with slightly different designs were fabricated to demonstrate the multiple wavelength emission capability of this integrated structure. Two surface emitting single-mode lasers derived from the same in-plane laser with a wavelength separation of 0.8nm was obtained.

5.2 Fabrication of Photonic Crystal Nanocavity Lasers

Our devices were fabricated on a 3-inch n⁺-GaAs wafer. Strained InGaAs/GaAs single quantum well structure grown by metal organic chemical vapor deposition (MOCVD) emitting at wavelength of 990nm was used as the lasing media. The grown layer structure consists of (from the substrate) (a) an n-Al_{0.3}Ga_{0.7}As cladding layer (thickness t=750nm), (b) an Al-rich Al_{0.9}Ga_{0.1}As buffer layer (t=200nm), (c) a thin n-Al_{0.3}Ga_{0.7}As cladding layer (t=200nm), (d) an undoped active region composed of a 10nm In_{0.2}Ga_{0.8}As sandwiched by two 200nm GaAs space layers, (e) a 1.15μm-thick p-Al_{0.3}Ga_{0.7}As cladding layer, and (f) a p⁺-GaAs Ohmic contact layer (t=120nm), as depicted in Fig. 5.1.

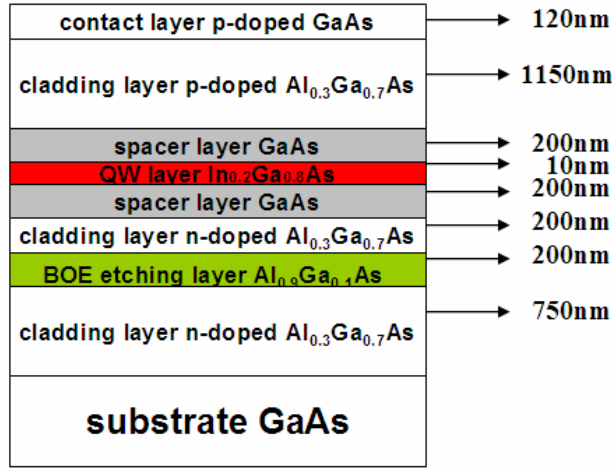


Fig. 5.1 Strained InGaAs/GaAs single quantum well laser structures. The emission wavelength is 990nm.

The process flow of an integrated PhC nanocavity coupled laser structure is shown in Fig. 5.2. Device fabrication began with strip patterns for the following mesa formation by using photolithography. Then, *p*-type metal films (Ti/Pt/Au=300/300/1500Å) were deposited with the help of E-Gun evaporator. After that, self-aligned ridge mesa was formed by chemical wet etching with a blend of solution H₂SO₄:H₂O₂:H₂O = 1:8:40 and stopped in the upper cladding layer of the laser structure. The ridge mesa has a length of 1500μm, a width of 20μm, and a height of 1.1μm and was used as the Fabry-Perot laser cavity. While one end of the ridge was a cleaved facet, the other end was a 2D PhC slab, which was used as the other mirror of the laser [77]. Next, a 320nm thickness of SiN film, serving as a hard mask for the following photonic crystal patterning, was deposited by the use of plasma enhanced chemical vapor deposition (PECVD) system. The photonic crystal was designed in hexagonal arrays with a period $a= 260\text{nm}$ and a hole diameter $2r = 165\text{nm}$. The PhC mirror had a length of 30μm and started at 8μm away from the edge of the ridge mesa. The holes in the PhC were defined on a 230nm thickness of PMMA resist by E-beam

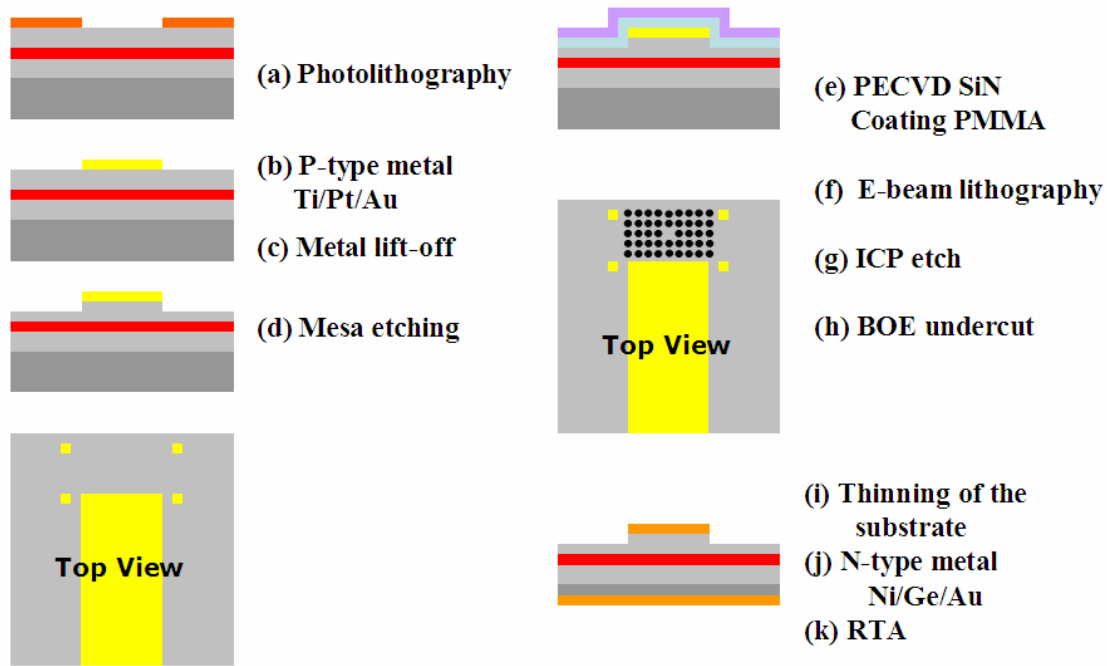


Fig. 5.2 Process flow of integrated photonic crystal nanocavity lasers.

lithography, followed by two runs of inductively coupled plasma reactive ion etch (ICP-RIE). The first round was aimed to transfer patterns from PMMA layer to SiN by using CHF_3/O_2 , and the second one lay in creating air holes from SiN to the epied wafer by using SiCl_4/Ar . The etching went through the laser's active layer and the confining layer and stopped at an $\text{Al}_{0.9}\text{Ga}_{0.1}\text{As}$ sacrificial layer. The slab was then formed by undercutting the sacrificial layer using a selective chemical etch, buffered HF (BOE), through the holes. The thickness of the slab was 600nm and the air gap was 200nm. The layer thicknesses used here were chosen for the convenience of fabrication and are probably not optimized for the PhC slab and the nanocavity. But since the cavity is placed quite close to the end of the laser ridge, the effect of the layer thickness on the nanocavity's performance is limited. Finally, *n*-Ohmic contact was deposited on the backside of substrate with Ni/Ge/Au (300/300/1500 Å) alloyed metallization. The fabricated schematic device and the scanning electron microscopy

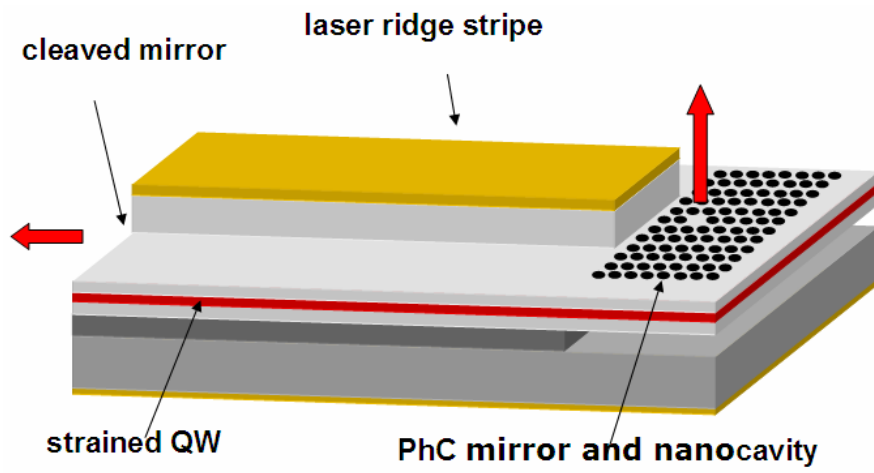


Fig. 5.3 Schematic of an integrated nanocavity coupled surface emitting laser.

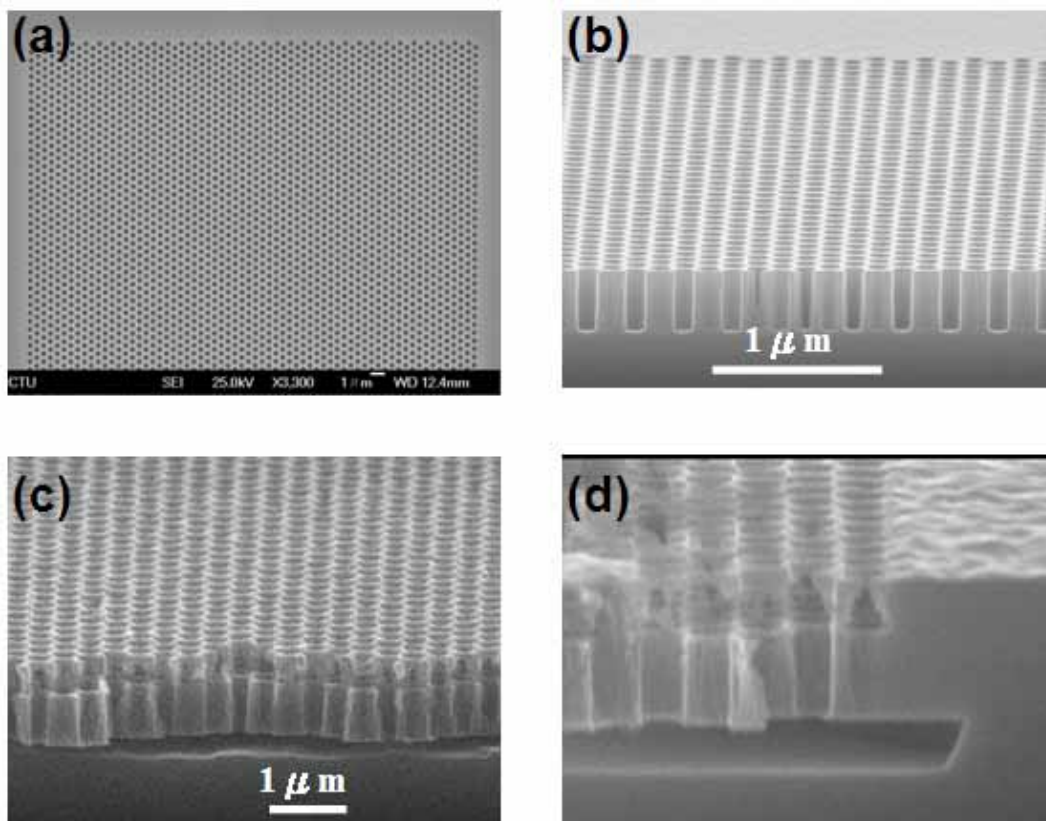


Fig. 5.4 SEM micrographs of completed photonic crystals. (a) and (b) are the photos taken from the top and the cross-section of samples, respectively. (c) shows the formed slab structure after BOE selective etching. (d) is a magnification view of (c).

(SEM) micrographs of defined photonic crystal slab are shown in Fig. 5.3 and 5.4, respectively.

5.3 Nanocavity Design

The PhC nanocavities were placed at the sixth row of the lattice from the edge of the PhC mirror. The position was chosen to ensure a good coupling from the laser light and a good Q factor for the nanocavities. The light intensity and its line shape of the trapped light in a single defect cavity as a function of its position are calculated by the 2D finite-difference time-domain (FDTD) method and shown in Fig. 5.5. Clearly a trade off between the coupling efficiency and the Q factor has to be considered. Based on the calculated result, the location at the sixth row appears to be the best for both light coupling and Q factor.

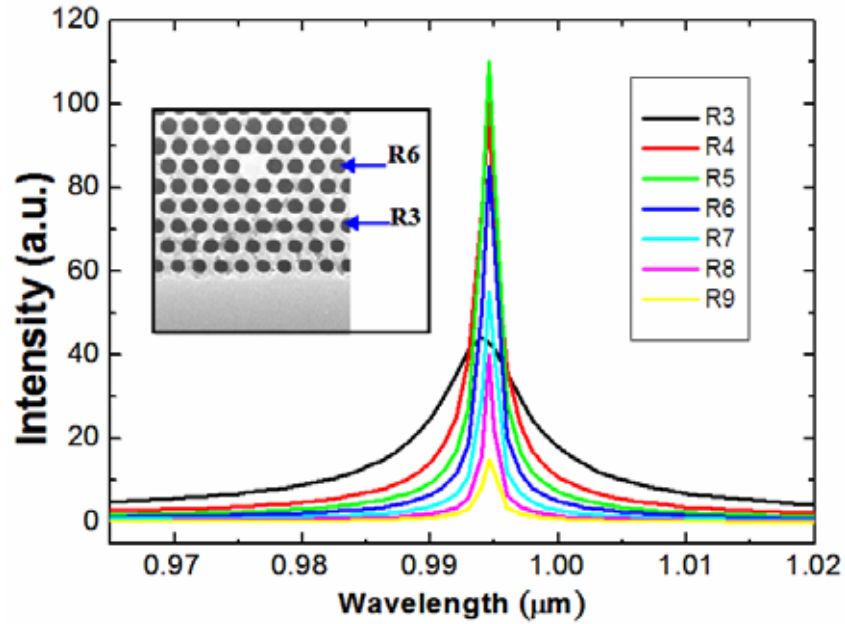
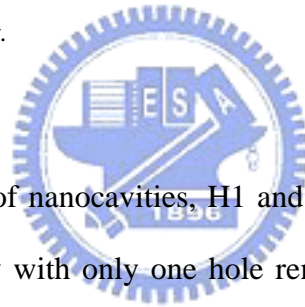


Fig. 5.5 Calculated position dependence of coupled output light intensity from an H1 nanocavity. The R_n ($n=1, 2, \dots, 9$) represents the row from which a hole is removed. The inset shows the position of a fabricated H1 cavity at the sixth row.



Lasers with two types of nanocavities, H1 and H2, were fabricated, where H1 being the single defect cavity with only one hole removed and H2 being the cavity with seven holes removed, as shown in the inset of Fig. 5.6. Guided by the calculation result shown in Fig. 5.5, we placed the cavities at the sixth row of the PhC mirror for optimum light coupling. Numerical calculation of the band structure and the field distribution profiles indicate that there are multiple resonant modes in the H1 and H2 cavities, as shown in Fig. 5.6. Within the laser's gain bandwidth, however, only dipole mode for the H1 and monopole mode for the H2 are considered (see Fig. 5.7).

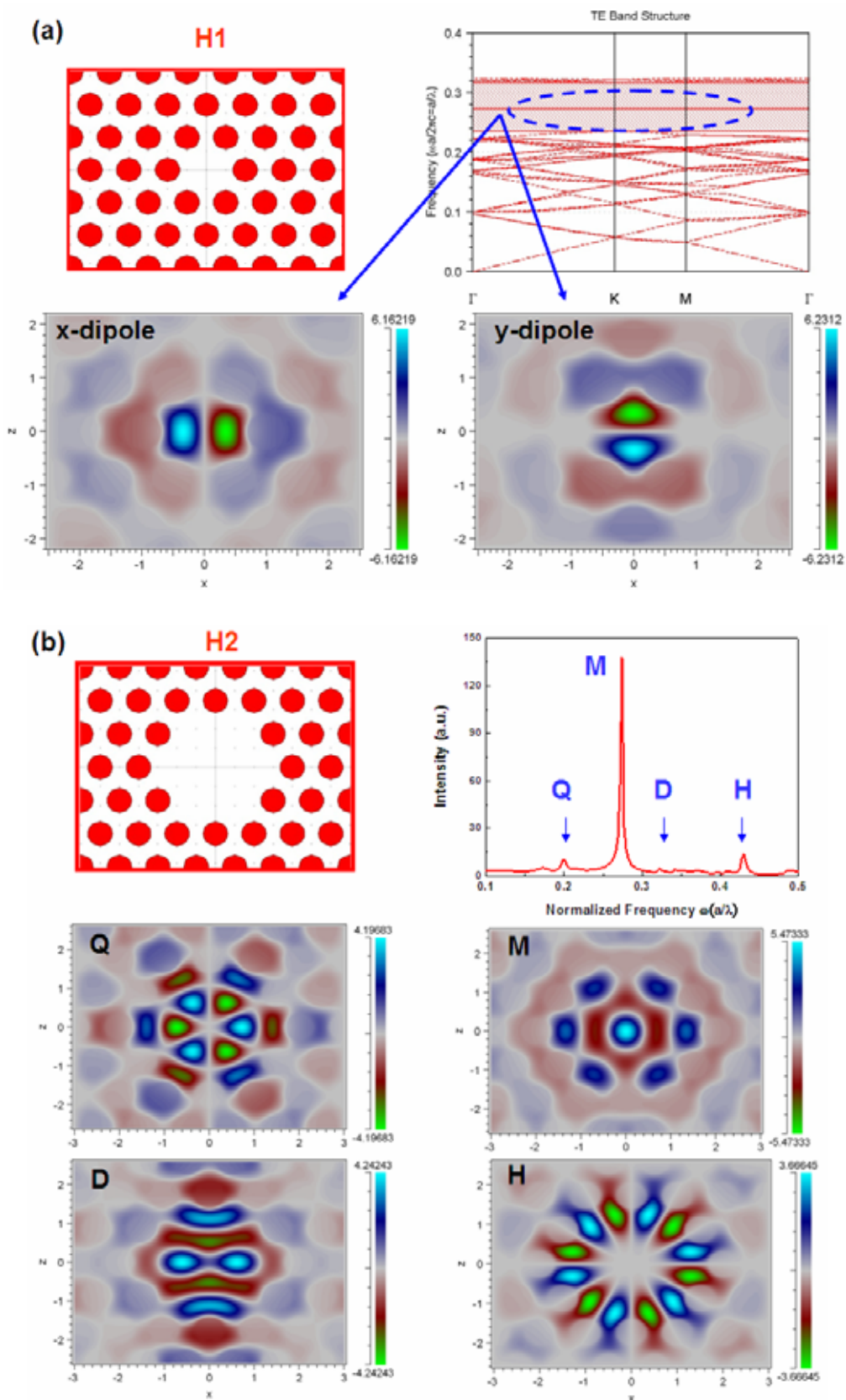


Fig. 5.6 Resonant cavity modes calculated by 2D plane wave expansion method and FDTD method. (a) Degenerated dipole modes exist in the H1 nanocavity. (b) Four different cavities modes, marked as Q, M, D, and H, in the H2 cavity.

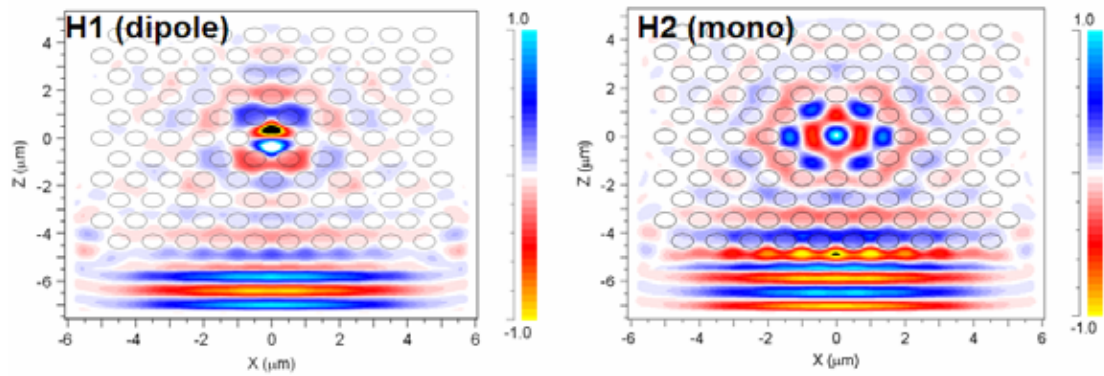


Fig. 5.7 Coupled cavity modes simulated by 2D FDTD method. A Gaussian wave with central wavelength of 990nm was launched into the photonic crystal region in the both cases. Due to the coupling effect, a degenerated dipole mode for H1 cavity (left) and a mono mode for H2 cavity (right) are excited, respectively.

5.4 Characteristics of Nanocavity Lasers



Device characterization is performed at room temperature under electrical pumping. A pulse with a 5% duty cycle is chosen to minimum the heat effect. The schematic diagram of the measurement system can be referred to [78]. The spectrum of the laser light emitted from the PhC nanocavity is very different from that measured from the cleaved facet of the laser diode. The nanocavity only picks up the resonant mode with a specific wavelength from the relatively wide laser spectrum. Figure 5.8(a), for example, shows the top view of the fabricated laser device with an integrated H1 cavity. When this sample is biased at above-threshold condition of lasing, a bright light emitted from the H1 cavity can be clearly seen, as shown in Fig. 5.8(b). Figure 5.8(c) shows its corresponding spectrum where the emission peak is at 992.8nm.

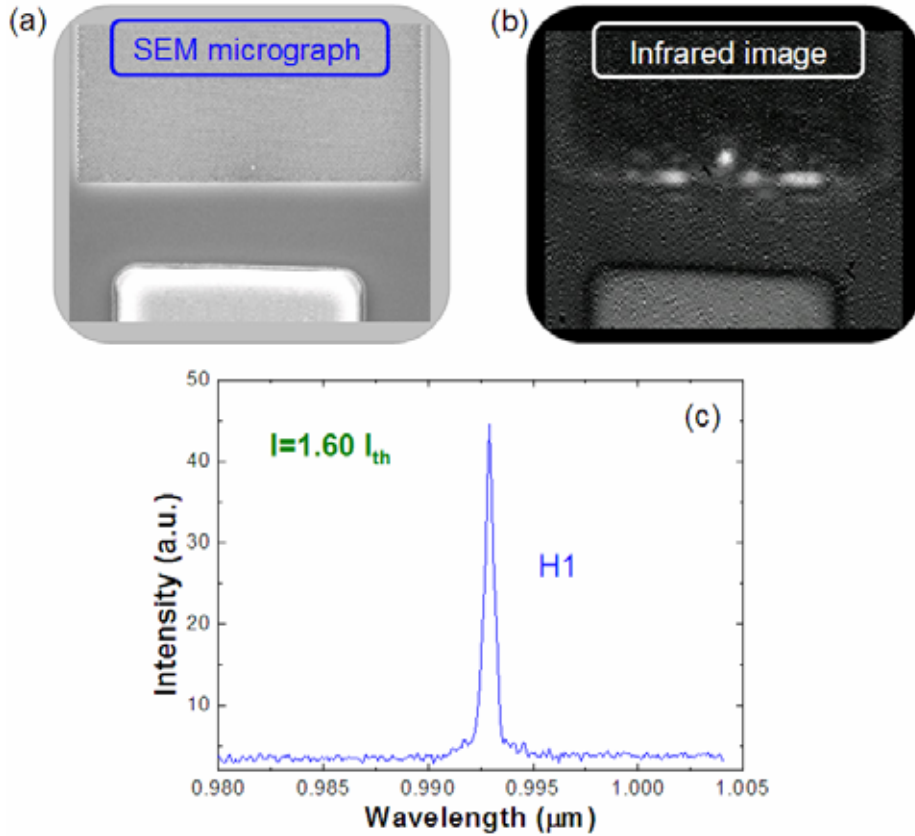


Fig. 5.8 (a) Top view of the fabricated sample with an integrated H1 cavity. (b) Infrared image taken from the H1 cavity. (c) Emission spectrum from the H1 cavity.

The emission spectrum from the cleaved mirror of the laser with the H1 cavity was also measured. As can be seen in Fig. 5.9, the emission spectra become broadened as the injection current increases. Of interest is a shallow dip that appears in the plots. Compare these spectra with that obtained from the H1 cavity, we found that this clear dip is exactly at the same position of the H1 cavity emission's peak, as shown in Fig. 5.10. Obviously, it demonstrates that part of the laser power is taken away by the resonant mode of the nanocavity. This phenomenon can be understood by the reflectivity of the PhC with the nanocavity. Because part of the light is coupled into the resonant mode of the nanocavity, the reflectivity spectrum shows a dip at the resonant wavelength and this results in a reduced emission intensity for the laser light from the cleaved mirror at that wavelength.

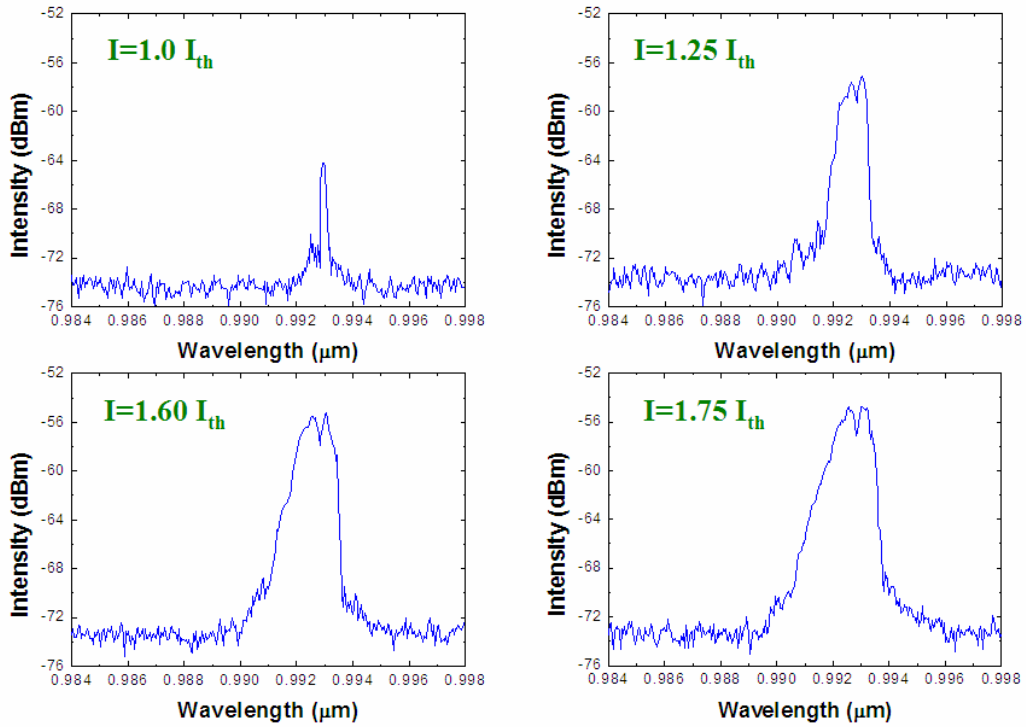


Fig. 5.9 Emission spectra measured from the cleaved facet of the laser with the integrated H1 cavity at different bias condition. Note that a clear dip appears as injection current is increasing.

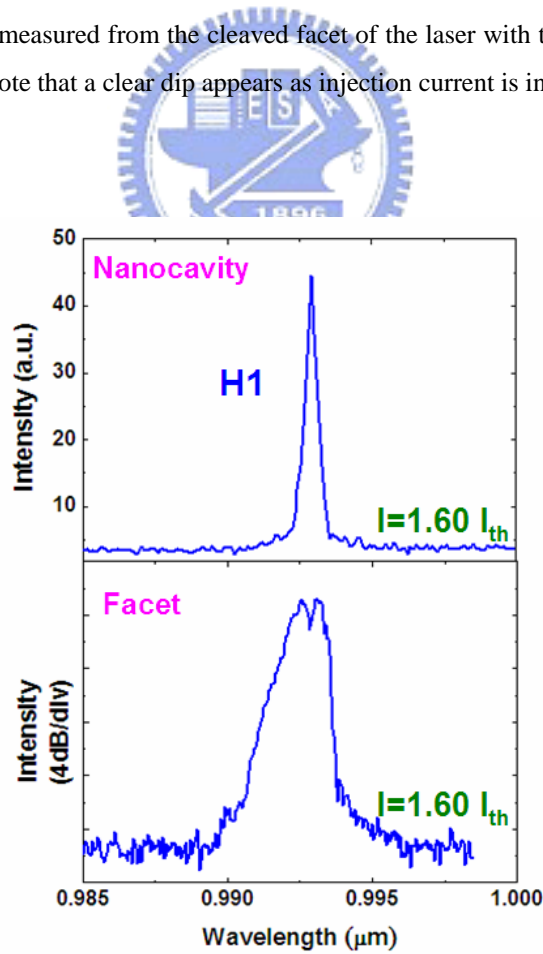


Fig. 5.10 For comparison, emission spectra from the H1 cavity and cleaved facet are put together. Obviously, the shallow dip is exactly at the same position of H1 cavity's emission peak.

Curves of the light output against injection current from the nanocavity for lasers integrated with H1 and H2 are shown in Fig. 5.11. Clearly the H2 cavity had a higher external quantum efficiency and a slightly higher threshold current than the H1 cavity. This is understandable because the H2 cavity, due to a larger size, has a higher coupling efficiency than the H1 cavity. The increased output coupling in turn causes a slight reduction in the reflectivity of the PhC mirror, and that contributes to the increase of the threshold current.

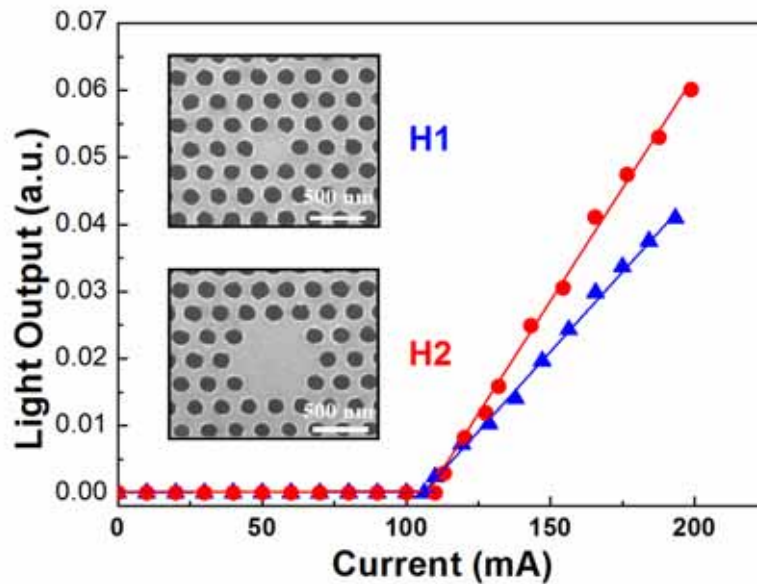


Fig. 5.11 *L-I* curves of laser emission from the H1 (blue triangle) and H2 (red dot) cavities.

Figure 5.12 shows the spectrum measured from a laser with an H1 cavity and that from a laser with an H2 cavity. The spectrum measured from the H1 cavity peaks at $\approx 992.8\text{nm}$ and has a linewidth of 0.526nm . The emission from the H2 cavity peaks at a slightly longer wavelength but has a much narrower width of only 0.26nm . From the line widths obtained, we calculated the Q factors for the H1 and H2 cavities to be 1890 and 3800, respectively. The higher Q for the H2 nanocavity is due to its

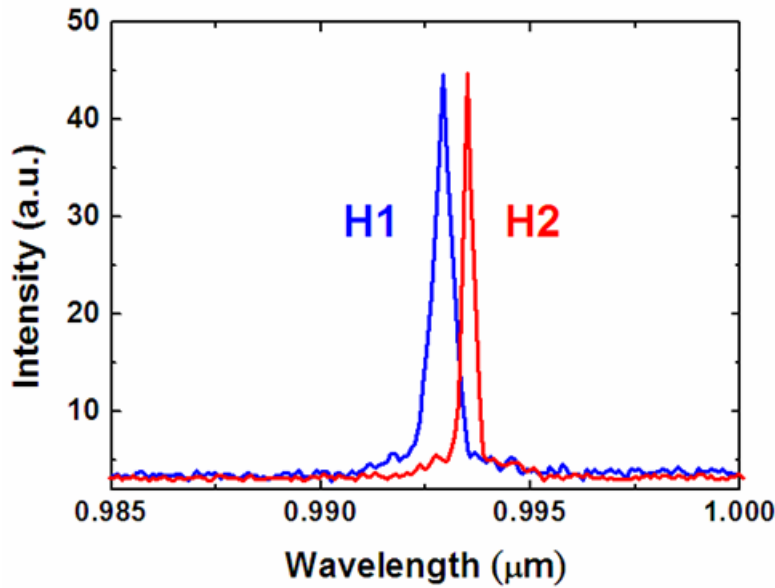


Fig. 5.12 Spectra measured from the H1(blue) and H2 (Red) nanocavities. The line width of the H1 and H2 emission peaks are 0.526nm and 0.26nm, respectively

non-degenerate monopole mode.

The temperature dependence of the emission peak from a laser with an H1 nanocavity and that of a laser without the photonic crystal mirror were also investigated. Figure 5.13 shows the emission spectra of our regular QW laser (without photonic crystal mirror) at different temperature. The emission peak shifts toward longer wavelength as temperature is increasing due to the band gap narrowing effect. Similarly, the temperature stability of the H1 cavity's emission peak is measured and compared with that of the regular QW lasers, as shown in Fig. 5.14. Apparently, the temperature sensitivity of the emission peak from the photonic crystal nanocavities is much better than that from the cleaved facet of FP lasers without any PhC structures. The amount of wavelength shift per for the regular laser is $0.45\text{nm}/^{\circ}\text{C}$, but that from the H1 nanocavity is only $0.097\text{nm}/^{\circ}\text{C}$. There is nearly a five times difference between the two. This also demonstrates the advantage of using the photonic crystal nanocavity as the light source.

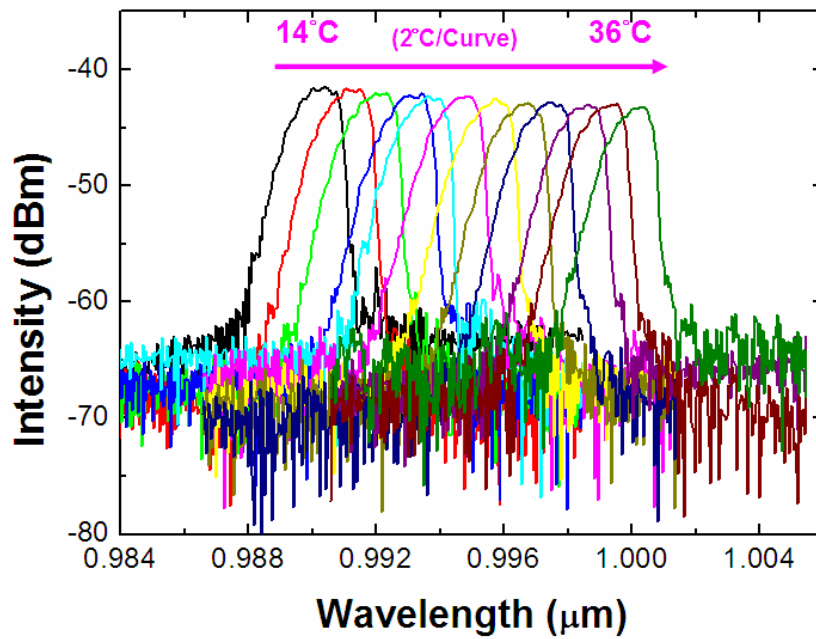


Fig. 5.13 Emission spectra measured from the regular QW laser at different operation temperature.

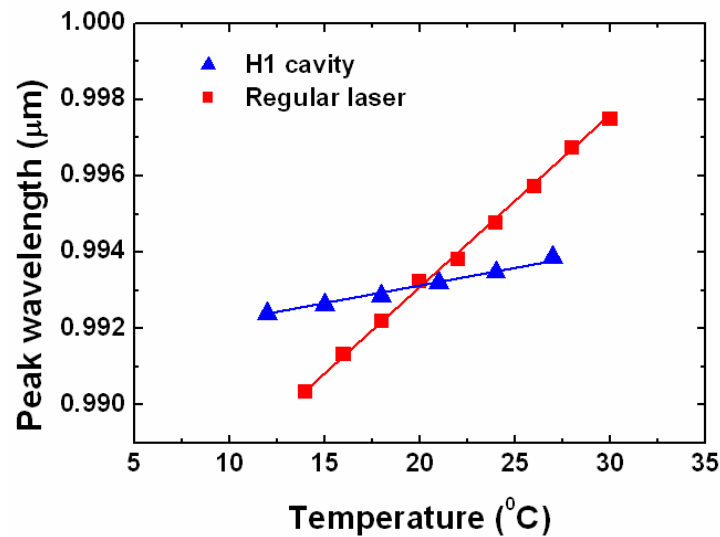


Fig. 5.14 Temperature dependence of the peak wavelength of the laser light measured from an H1 nanocavity and that of the regular laser light measured from the cleaved facet. The slopes of these two lines are $0.097 \text{ nm}^\circ\text{C}$ (blue triangle) and $0.45 \text{ nm}^\circ\text{C}$ (red square), respectively.

Since the emission wavelength of PhC nanocavities can be easily tuned by cavity design, we are able to shift the resonant wavelength of the cavity continuously by slightly adjusting the size of the inner most holes of a cavity. Figure 5.15(a) shows the calculated wavelength shift of an H2 nanocavity. The rate of shift, $\Delta\lambda/2\Delta r'$, is -1.08nm/nm . Based on this result, we designed two H2 nanocavities side by side. The cavities had $a=260\text{nm}$, $2r_0 = 166\text{nm}$. One of the cavities had all the surrounding holes the same dimension as the rest of the holes in the photonic crystal, while the other one had the surrounding holes (the inner most holes) slightly smaller with the diameter $2r'=165.2\text{nm}$.

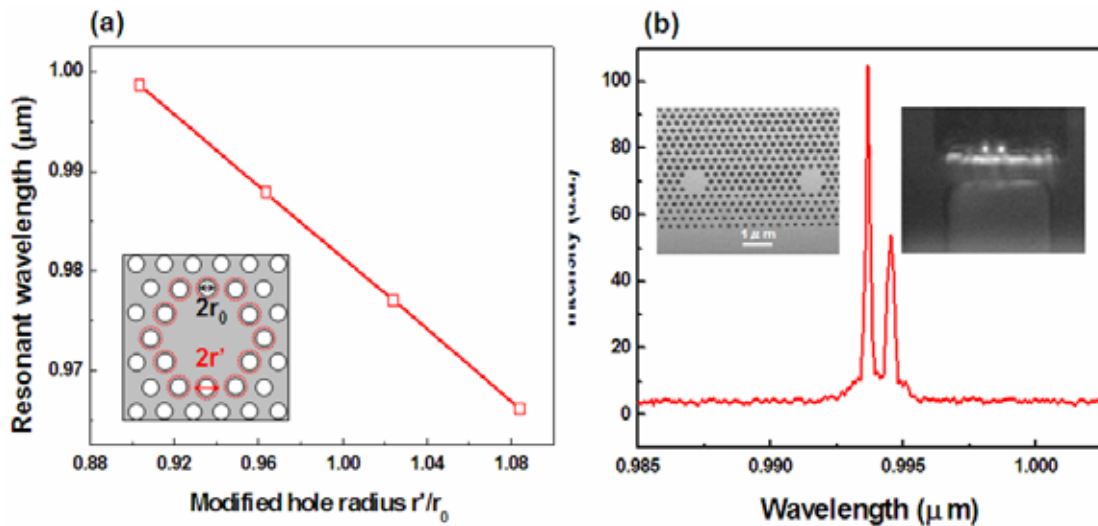


Fig. 5.15 (a) Resonant wavelength as a function of holes radius in modified H2 nanocavities. The inset depicts that 12 inner most holes are modified in diameter. $2r_0$ and $2r'$ denote the diameter of the regular holes and modified inner most holes, respectively. (b) Measured spectrum of the laser light from the two nanocavities. The inset: (Left) SEM micrograph of two side-by-side modified H2 PhC nanocavities. (Right) Infrared image of laser emission from the two nanocavities.

The left and right insets in Fig. 5.15(b) show the SEM micrograph of the two fabricated nanocavities and the infrared image of the surface emitting laser beam from these nanocavities. Also, the spectrum of the laser light from the two cavities is shown

in Fig. 5.15(b). Two narrow emission peaks corresponding to the two cavities at 993.4nm and 994.2nm are clearly seen. The separation of the two peaks is 0.8nm.

5.5 Summary

In conclusion, we have fabricated an integrated PhC nanocavity-laser structure. The 2D PhC slab was used as one of the reflective mirrors for the laser cavity, while the nanocavity in the photonic crystal served as a coupling outlet for the surface emitting laser light. In this manner, an electrically driven laser light was converted to a surface emitting laser light with a narrow spectrum. Both H1 and H2 nanocavities have been fabricated. Single mode emission with high Q factors [$Q(H1)=1890$ and $Q(H2)=3800$] was obtained. Excellent temperature stability ($0.097\text{nm}/^\circ\text{C}$) of the laser emission from the nanocavity was observed as well. We have also demonstrated the multiple wavelength emission capability of this integrated structure by utilizing two PhC nanocavities with slightly different designs. Two single modes, narrow line width surface emitting laser lights were obtained.

Chapter 6

Conclusion and Suggestion

6.1 Conclusion

We have reported on the theoretical analyses and experimental measurements of group velocities of light propagation in photonic crystal waveguides for the promising applications of all-photonic integrated circuits and optical delay lines. We also demonstrated an electrically-driven integrated photonic crystal nanocavity coupled surface emitting laser as a potential candidate for single mode emission light sources.

The primary results in this dissertation are summarized as follows:

1. 2D slab of W1 type photonic crystal waveguides were fabricated on SOI wafers. The ingenious design in crystal patterns and superior technology in sample fabrication enabled us to obtain a very small propagation loss ($\sim 2\text{-}3\text{dB/mm}$) of the waveguides. The measured transmission spectra displayed unusual Fabry-Perot oscillation peaks near the cutoff region. By the use of Fabry-Perot formula, the group index exceeding 200 was obtained. Results from the phase delay measurement on the propagation of modulated light waves within the waveguides also showed large group indices at the position close to the zone edge. These values fit well with the theoretical group velocities calculated from the defect bands of the waveguides.
2. For the first time, 2D photonic crystal coupled waveguides, composed of two parallel W1 type photonic crystal waveguides, were successfully fabricated. The integrated MMI devices were used to excite and collect coupled modes. The theoretical unique flat band (inflection point) of

coupled modes allowing slow light mode propagation was investigated by means of frequency domain and time domain approaches. A sharp dip in the middle of transmission spectrum and the peaking of the group index from the Mach-Zehnder interference measurement clearly indicated the existence of such inflection point. The time-of-flight optical pulses of 24~28 ps (FWHM) recorded on a high speed oscilloscope also obviously displayed an extremely small group velocity of $0.017c$ at a wavelength of $\lambda=1537.30$ nm, which corresponds to the inflection-point slow light modes.

3. Single mode emission lasers with photonic crystal nanocavities integrated with electrically-driven quantum well edge-emitting laser diodes were demonstrated. The photonic crystal served as an end mirror for the laser cavity, while the nanocavities served as wavelength selective high-Q surface emitters. From the lasing spectra, high Q factors of 1890 for the H1 cavity and 3800 for the H2 cavity were observed. The laser emission from the nanocavities had excellent temperature stability ($0.097\text{nm}/^\circ\text{C}$). The wavelength shift versus temperature was about five times better than that of regular quantum well lasers. Dual wavelength emission from two side by side slightly different cavities was also demonstrated. Laser emission with two wavelengths of $\Delta\lambda = 0.8\text{nm}$ was obtained.

6.2 Suggestion for Future Work

An ideal optical buffer device in the optical communication network should possess the properties of *low loss*, *zero dispersion*, *large delay time*, and *broad bandwidth* for launched light waves. In this dissertation, photonic crystal waveguides were shown to

have great ability to slow down the light waves. Also, a small propagation loss of (2~3dB/mm) was reported. However, these are not good enough for the application to industry because of large dispersion and loss of the band-edge guided modes. Therefore, for industrial purposes, how to manage pulse dispersion and diminish propagation loss should be the main issues.

Photonic crystal coupled waveguide is one of the solutions, as it makes possible for light waves to propagate at very slow speed and small velocity dispersion due to the unique S-shaped band structure. But the constant of formulated delay-bandwidth product leads to another trade-off problem: the larger the delay time, the smaller the bandwidth. As can be seen in Chapter 5, the observed inflection-point slow light modes correspond to a narrow bandwidth of only 2nm. This would limit the practicability in the development of photonic integrated circuits. One of the most suggested approaches is to employ the chirped refractive index on the photonic crystal waveguides [52, 61]. But this is merely theoretical proposal and may not be easy to carry out by the existing fabrication technology. So, more efforts still have to be made to achieve small group velocity and broad bandwidth for propagation waves in the photonic couple waveguides.

As for the electrically-driven integrated photonic crystal nanocavity lasers, quantum dots as an active medium should be recommended for the enhancement of the coupling probability between cavity modes and lasing modes because of its broadening emission spectrum. To achieve very high Q value (i.e. $Q > 10,000$), the structure of the fabricated slab and the pattern of the nanocavities should be optimized. The design rules can be referred to the published results on nanocavities, which have demonstrated Q value exceeding hundred thousands under optical pumping or coupling operation [18-19, 64]. Furthermore, the integrated nanocavities can be replaced by (or combined with) photonic crystal waveguides to become

multi-function photonic integrated circuits. These circuits would no longer need a passive waveguide and an external light source. Instead, the integrated electrical pumping edge-emitting laser diode directly provides essential optical waves. Once the laser is driven by injection current, each component of the photonic circuit would start to work accordingly. This image would be very similar to an electronic chip, and can be named “photonic chips”. To realize this, experiments on the integrated W1 type photonic crystal waveguides should be expected.



Reference:

1. E. Yablonovitch, "Inhibited spontaneous emission in solid-state physics and electrics," *Phys. Rev. Lett.* **58**, 2059 (1987).
2. S. John, "Strong localization of photons in certain disordered dielectric superlattices," *Phys. Rev. Lett.* **58**, 2486 (1987).
3. K. M. Ho, C. T. Chan, and C. M. Soukoulis, "Existence of a photonic gap in periodic dielectric structures," *Phys. Rev. Lett.* **65**, 3152 (1990).
4. E. Yablonovitch, T. J. Gmitter, and K. M. Leng, "Photonic band structure: The face-center-cubic case employing nonspherical atoms," *Phys. Rev. Lett.* **67**, 2295 (1991).
5. S. Y. Lin, J. G. Fleming, D. L. Hetherington, B. K. Smith, R. Biswas, K. M. Ho, M. M. Sigalas, W. Zubrzycki, S. R. Kurtz, and Jim Bur, "A three-dimensional photonic crystal operating at infrared wavelengths," *Nature* **394**, 251 (1998).
6. S. Noda, N. Yamamota, H. Kobayashi, M. Okano, and K. Tomoda, "Optical properties of three-dimensional photonic crystals based on III-V semiconductors at infrared to near-infrared wavelengths," *Appl. Phy. Lett.* **75**, 905 (1999).
7. R. D. Meade, K. D. Brommer, A. M. Rappe, and J. D. Joannopoulos, "Existence of a photonic band gap in two dimensions," *Appl. Phy. Lett.* **61**, 495 (1992).
8. T. F. Krauss, Y. P. Song, S. Thoms, C. D. W. Wilkinson, and R. M. DeLaRue, "Fabrication of 2-D photonic bandgap structures in GaAs/AlGaAs," *Electron. Lett.* **30**, 1444 (1994).
9. T. F. Krauss, R. M. De La Rue, and S. Brand, "Two-dimensional photonic-bandgap structures operating at near-infrared wavelengths," *Nature* **383**, 699 (1996).
10. O. Painter, R. K. Lee, A. Scherer, A. Yariv, J. D. O'Brien, P. D. Dapkus, and I. Kim, "Two-dimensional photonic band-gap defect mode laser," *Science* **284**, 1819 (1999).
11. S. Noda, M. Yokoyama, M. Imada, A. Chutinan, and M. Mochizuki, "Polarization mode control of two-dimensional photonic crystal laser by unit cell structure design," *Science* **293**, 1123 (2001).
12. R. F. Cregan, B. J. Mangan, J. C. Knight, T. A. Birks, P. St. J. Russell, P. J. Roberts, and D. C. Allan, "Single-mode photonic band gap guidance of light in air," *Science* **285**, 1537 (1999).
13. M. Notomi, "Theory of light propagation in strongly modulated photonic crystals: refraction-like behavior in the vicinity of the photonic band gap," *Phys. Rev. B.* **62**, 10696 (2000).

14. T. Yoshie, A. Scherer, J. Hendrickson, G. Khitrova, H. M. Gibbs, G. Rupper, C. Ell, O. B. Shchekin, and D. G. Deppe, "Vacuum Rabi splitting with a single quantum dot in a photonic crystal nanocavity," *Nature* **432**, 200 (2004).
15. H. Gersen, T. J. Karle, R. J. P. Engelen, W. Bogaerts, J. P. Korterik, N. F. van Hulst, T. F. Krauss, and L. Kuipers, "Real-space observation of ultraslow light on photonic crystal waveguides," *Phys. Rev. Lett.* **94**, 073903 (2005).
16. M. F. Yanik and S. Fan, "Stopping light all-optically," *Phys. Rev. Lett.* **92**, 083901 (2004).
17. M. Notomi, K. Yamada, A. Shinya, J. Takahashi, C. Takahashi, and I. Yokohama, "Extremely large group velocity dispersion of line-defect waveguides in photonic crystal slabs," *Phys. Rev. Lett.* **87**, 253902 (2001).
18. H. Y. Ryu, H. G. Park, and Y. H. Lee, "Two-dimensional photonic crystal semiconductor lasers: Computational design, fabrication, and characterization," *IEEE Selected Topics in Quantum Electronics* **8**, 891 (2002).
19. B. S. Song, S. Noda, T. Asano, and Y. Akahane, "Ultra-high-Q photonic double-heterostructure nanocavity," *Nature Materials* **4**, 207 (2005).
20. E. Kuramochi, M. Notomi, S. Mitsugi, A. Shinya, T. Tanabe, and T. Watanabe, "Ultrahigh-Q photonic crystal nanocavities realized by the local width modulation of a line defect," *Appl. Phys. Lett.* **88**, 041112 (2006).
21. J. D. Jackson, *Classical Electrodynamics*, John Wiley & Sons Publisher (1962).
22. D. K. Cheng, *Field and Wave Electromagnetics 2nd Edition*, Addison Wesley Publishers (1989).
23. J. D. Joannopoulos, R. D. Meade, and J. N. Winn, *Photonic Crystals: Modeling the Flow of Light*, Princeton Publishers (1995).
24. K. Sakoda, *Optical Properties of Photonic Crystals*, Springer Publishers (2001).
25. N. W. Ashcroft and N. D. Mermin, *Solid State Physics*, Thomson Publishers (1976)
26. C. Kittel, *Introduction to Solid State Physics 7th Edition*, John Wiley & Sons Publishers (1996).
27. K. M. Leung and Y. F. Liu, "Full vector wave calculation of photonic band structures in face-centered-cubic dielectric media," *Phys. Rev. Lett.* **65**, 2646 (1990).
28. S. Noda and T. Baba, *Roadmap on Photonic Crystals*, Kluwer Academic Publishers (2003).
29. A. J. Danner, "An introduction to the plane wave expansion method for calculating photonic crystal band diagrams," *Ph.D. dissertation*, University of Illinois at Urbana-Champaign, Urbana (2005).
30. A. Tavlove, *Computational Electrodynamics: The Finite-Difference Time Domain Method*, Artech House Publishers (1995).

31. K. Yee, "Numerical solution of initial boundary value problems involving Maxwell's equations in isotropic media," *IEEE Trans. on Antennas and Propagation* **14**, 302 (1966).
32. J. P. Berenger, "Three-dimensional perfectly matched layer for the absorption of electromagnetic waves," *J. Comput. Phys.* **127**, 363 (1996).
33. Software package, *Bandsolve v1.3* and *Fullwave v3.0.1*, Rsoft Design Group, Inc. (2003).
34. W. M. Robertson, G. Arjavalingham, R. D. Meade, K. D. Brommer, A. M. Rappe, and J. D. Joannopoulos, "Measurement of photonic band structure in a two-dimensional periodic dielectric array," *Phys. Rev. Lett.* **68**, 2023 (1992).
35. K. Sakoda, "Measurement of photonic band structure in a two-dimensional periodic dielectric array," *Phys. Rev. B* **51**, 4672 (1995).
36. E. Yablonovitch, T. J. Gmitter, and K. M. Leung, "Donor and acceptor modes in photonic band structure," *Phys. Rev. Lett.* **67**, 3380 (1991).
37. O. J. Painter, A. Husain, A. Sherer, J. D. O'Brien, I. Kim, and P. D. Dapkus, "Room temperature photonic crystal defect lasers at near-infrared wavelengths in InGaAsP," *J. Lightwave Technol.* **17**, 2082 (1999).
38. J. K. Hwang, H. Y. Ryu, D. S. Song, I. Y. Han, H. W. Song, H. K. Park, and Y. H. Lee, "Room temperature triangular-lattice two dimensional photonic band gap lasers operating at 1.54 μm ," *Appl. Phys. Lett.* **76**, 2982 (2000).
39. K. Inoue and K. Ohtaka, *Photonic crystals*, Springer Publishers (2004).
40. M. Campbell, D. N. Sharp, M. T. Harrison, R. G. Denning, and A. J. Turberfield, "Fabrication of photonic crystals for the visible spectrum by holographic lithography," *Nature* **404**, 53 (2000).
41. E. Chow, S. Y. Lin, S. G. Johnson, P. R. Villeneuve, J. D. Joannopoulos, J. R. Wendt, G. A. Vawter, W. Zubrzycki, H. Hou, A. Alleman, "Three-dimensional control of light in a two-dimensional photonic crystal slab," *Nature* **407**, 983 (2000).
42. A. Shinya, M. Notomi, I. Yokohama, C. Takahashi, J. Takahashi, and T. Tamamura, "Two-dimensional Si photonic crystals on oxide using SOI," *Opt. Quantum Electron.* **34**, 113 (2002).
43. S. M. Sze, *Physics of Semiconductor Devices*, John Wiley and Sons Publishers (1981).
44. M. Lončar, D. Nedeljković, T. Doll, J. Vučković, A. Sherer, and T. P. Pearsall, "Waveguiding in planar photonic crystals," *Appl. Phys. Lett.* **77**, 1937 (2000).
45. S. Boscolo, M. Midrio, and T. F. Krauss, "Y junctions in photonic crystal channel waveguides: high transmission and impedance matching," *Opt. Lett.* **27**, 1001 (2002).

46. H. Takano, Y. Akahane, T. Asano, and S. Noda, "In-plane-type channel drop filter in a two-dimensional photonic crystal slab," *Appl. Phys. Lett.* **84**, 2226 (2004).
47. M. F. Yanik, S. Fan, and M. Soljacic, "High-contrast all-optical bistable switching in photonic crystal microcavities," *Appl. Phys. Lett.* **83**, 2739 (2003).
48. M. Qiu, "effective index method for heterostructure-slab-waveguide-based two-dimensional photonic crystals," *Appl. Phys. Lett.* **81**, 1163 (2002).
49. Kuramochi, 8p-H-3, JSAP autumn meeting (2005).
50. Y. A. Vlasov, M. O'Boyle, H. F. Hamann, and S. J. McNab, "Active control of slow light on a chip with photonic crystal waveguides," *Nature* **438**, 65 (2005).
51. R. S. Jacobsen, A. V. Lavrinenko, L. H. Frandsen, C. Peucheret, B. Zsigri, G. Moulin, J. Fage-Pedersen, and P. I. Borel, "Direct experimental and numerical determination of extremely high group indices in photonic crystal waveguides," *Opt. Express* **13**, 7861 (2005).
52. D. Mori and T. Baba, "Dispersion-controlled optical group delay device by chirped photonic crystal waveguides," *Appl. Phys. Lett.* **85**, 1101 (2004).
53. M. L. Povinelli, S. G. Johnson, J. D. Joannopoulos, "Slow-light, band-edge waveguides for tunable time delays," *Optics Express* **13**, 7145 (2005).
54. A. Yariv, Y. Xu, R. K. Lee, and A. Sherer, "Coupled-resonator optical waveguide: a proposal and analysis," *Opt. Lett.* **24**, 711 (1999).
55. T. J. Karle, D. H. Brown, R. Wilson, M. Steer, and T. F. Krauss, "Planar photonic crystal coupled cavity waveguides," *IEEE J. Select. Topics Quantum Electron.* **8**, 909 (2002).
56. M. F. Yanik, W. Suh, Z. Wang, and S. Fan, "Stopping light in a waveguide with an all-optical analog of electromagnetically induced transparency," *Phys. Rev. Lett.* **93**, 233903 (2004).
57. A. Y. Petrov and M. Eich, "Zero dispersion at small group velocities in photonic crystal waveguides," *Appl. Phys. Lett.* **85**, 4866 (2004).
58. J. Huang, C. M. Reinke, A. Jafarpour, B. Momeni, M. Soltani, and Ali Adibi, "Observation of large parity change-induced dispersion in triangular-lattice photonic crystal waveguides using phase sensitive techniques," *Appl. Phys. Lett.* **88**, 071111 (2006).
59. T. Asano, K. Kiyota, D. Kumamoto, B. S. Song, and S. Noda, "Time-Domain measurement of pico-second light propagation in a two-dimensional photonic crystal slab waveguide," *Appl. Phys. Lett.* **84**, 4690 (2004).
60. R. J. P. Engelen, Y. Sugimoto, Y. Watanabe, J. P. Korterik, N. Ikeda, N. F. van Hulst, K. Asakawa, and L. Kuipers, "The effect of high-order dispersion on slow light propagation in photonic crystal waveguides," *Opt. Express* **14**, 1658 (2006).

61. D. Mori and T. Baba, "Wideband and low dispersion slow light by chirped photonic crystal coupled waveguide," *Opt. Express* **13**, 9398 (2005).
62. N. Yamamoto, T. Ogawa, and K. Komori, "Photonic crystal directional coupler switch with small switching length and wide band width," *Opt. Express* **14**, 1223 (2006).
63. Y. A. Vlasov and S. J. McNab, "Coupling into the slow light mode in slab-type photonic crystal waveguides," *Optics Letters* **31**, 50 (2006).
64. Y. Akahane, T. Asano, B. S. Song, and S. Noda, "High-Q photonic nanocavity in a two-dimensional photonic crystal," *Nature* **425**, 944 (2003).
65. T. Tanabe, M. Notomi, E. Kuramochi, A. Shinya, and H. Taniyama, "Trapping and delaying photons for one nanosecond in an ultrasmall high-Q photonic crystal nanocavity," *Nature Photonics* **1**, 49 (2007).
66. E. M. Purcell, "Spontaneous emission probabilities at radio frequencies," *Phys. Rev.* **69**, 681 (1946).
67. J. Vučković, M. Lončar, H. Mabuchi, and A. Sherer, "Design of photonic crystal microcavities for cavity QED," *Phys. Rev. E* **65**, 016608 (2001).
68. H. Mabuchi and A.C. Doherty, "Cavity quantum electrodynamics: coherence in context," *Science* **298**, 1372 (2002).
69. J. Vučković and Y. Yamamoto, "Photonic crystal microcavities for cavity quantum electrodynamics with a single quantum dot," *Appl. Phys. Lett.* **82**, 2374 (2003).
70. T. Tanabe, M. Notomi, S. Mitsugi, A. Shinya, and E. Kuramochi, "Fast bistable all-optical switch and memory on a silicon photonic crystal on-chip," *Opt. Lett.* **30**, 2575 (2005).
71. S. Fan, P. R. Villeneuve, J. D. Joannopoulos, M. J. Khan, C. Manolatou, and H. A. Haus, "Theoretical analysis of channel drop tunneling processes," *Phys. Rev. B* **59**, 15882 (1999).
72. S. Fan, P. R. Villeneuve, J. D. Joannopoulos, and H. A. Haus, "Channel drop tunneling through localized states," *Phys. Rev. Lett.* **80**, 960 (1998).
73. A. Badolato, K. Hennessy, M. Atatüre, J. Dreiser, E. Hu, P. M. Petroff, and A. Imamoglu, "Deterministic coupling of single quantum dots to single nanocavity modes," *Science* **308**, 1158 (2005).
74. D. Englund, D. Fattal, E. Waks, G. Solomon, B. Zhang, T. Nakaoka, Y. Arakawa, Y. Yamamoto, and J. Vučković, "Controlling the spontaneous emission rate of single quantum dots in a two-dimensional photonic crystal," *Phys. Rev. Lett.* **95**, 013904 (2005).
75. W. H. Chang, W. Y. Chen, H. S. Chang, T. P. Hsieh, J. I. Chy, and T. M. Hsu, "Efficient single-photon sources based on low-density quantum dots in photonic crystal nanocavities," *Phys. Rev. Lett.* **96**, 117401 (2006).

76. H. G. Park, S. H. Kim, S. H. Kwon, Y. G. Ju, J. K. Yangatu, J. H. Baek, S. B. Kim, and Y. H. Lee, "Electrically driven single-cell photonic crystal laser," *Science* **305**, 1444 (2004).
77. T. D. Happ, M. Kamp, and A. Forchel, "Integration of 2D photonic crystals with ridge waveguide lasers," *Opt. Quantum Electron.* **34**, 91 (2004).
78. G. Lin, "Studies on semiconductor quantum structure lasers," *Ph. D. dissertation*, National Chaio Tung University, Hsinchu, Taiwan (2001).



Vita

Name : Shih-Chieh Huang (黃世傑)

Date of birth : June 27, 1978

Place of birth: Changhua, Taiwan, R.O.C.

Sex: Male

Education :

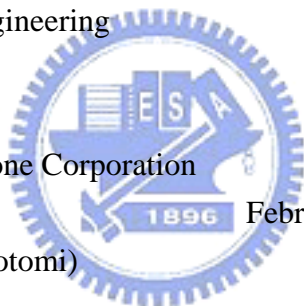
National Chiao Tung University Ph. D. September, 2002 — June, 2007
Institute of Electronics Engineering

National Chiao Tung University M. S. September, 2000 — June, 2002
Institute of Electronics Engineering

National Chiao Tung University B. S. September, 1996 — June, 2000
Department of Electronics Engineering

Internship:

Nippon Telegraph and Telephone Corporation
Basic Research Laboratories February, 2005 — September, 2006
(Group Leader: Dr. Masaya Notomi)



Title of Ph. D. Dissertation:

Study on Slow Light in Photonic Crystal Waveguides and Integrated Photonic Crystal Nanocavity Coupled Surface Emitting Lasers

Publication List

- [1] **S. C. Huang**, T. H. Yang, C. P. Lee, and S. D. Lin, "Electrically driven integrated photonic crystal nanocavity coupled surface emitter laser," *Appl. Phys. Lett.* **90**, 151121 (2007).
- [2] **S. C. Huang**, M. Kato, E. Kuramochi, C. P. Lee, and M. Notomi, "Time-domain and spectral-domain investigation of inflection-point slow light modes in photonic crystal coupled waveguides," *Opt. Express* **15**, 3543 (2007).
- [3] **S. C. Huang**, T. H. Yang, C. P. Lee, and S. D. Lin, "Single mode operation of integrated photonic crystal nanocavity coupled surface emitting lasers," JMB6, CLEO/QELS'07, Baltimore, U. S. A. (2007).
- [4] **S. C. Huang**, M. Kato, E. Kuramochi, C. P. Lee, and M. Notomi, "Experimental observation of inflection-point slow light modes in photonic crystal coupled waveguides," CMV6, CLEO/QELS'07, Baltimore, U. S. A. (2007).
- [5] Y. H. Zhang, T. Tawara, N. Cade, D. Ding, T. Tanabe, E. Kuramochi, S. R. Johnson, **S. C. Huang**, and M. Notomi, "GaAs based InAs Quantum Dot Photonic Crystal Lasers," SPIE Photonics West, San Jose CA, U. S. A. (2007).
- [6] M. Kato, **S. C. Huang**, E. Kuramochi, and M. Notomi, "Time-domain measurement of slow light in photonic crystal coupled waveguide," JSAP Spring Meeting, Japan (2007).
- [7] K. W. Sun, **S. C. Huang**, A. Kechiantz, and C. P. Lee, "Subwavelength gratings fabricated on semiconductor substrates via E-beam lithography and lift-off method," *Optical and Quantum Electronics* **37**, 425 (2005).
- [8] **S. C. Huang**, E. Kuramochi, T. Watanabe, C. P. Lee, and M. Notomi, "Group delay analysis of low-loss Si photonic crystal waveguides," JSAP Autumn Meeting, Japan (2005).
- [9] H. M. Lee, E. Y. Chang, S. Chen, and **S. C. Huang**, "50-nm-T-gate fabricated by thermally reflowed resist technique", SPIE Microlithography, Santa Clara, California U. S. A. (2003).